Modeling the performance and emissions of a steam injected water recovering turbofan engine

MSc Thesis Report

Adnan Feim

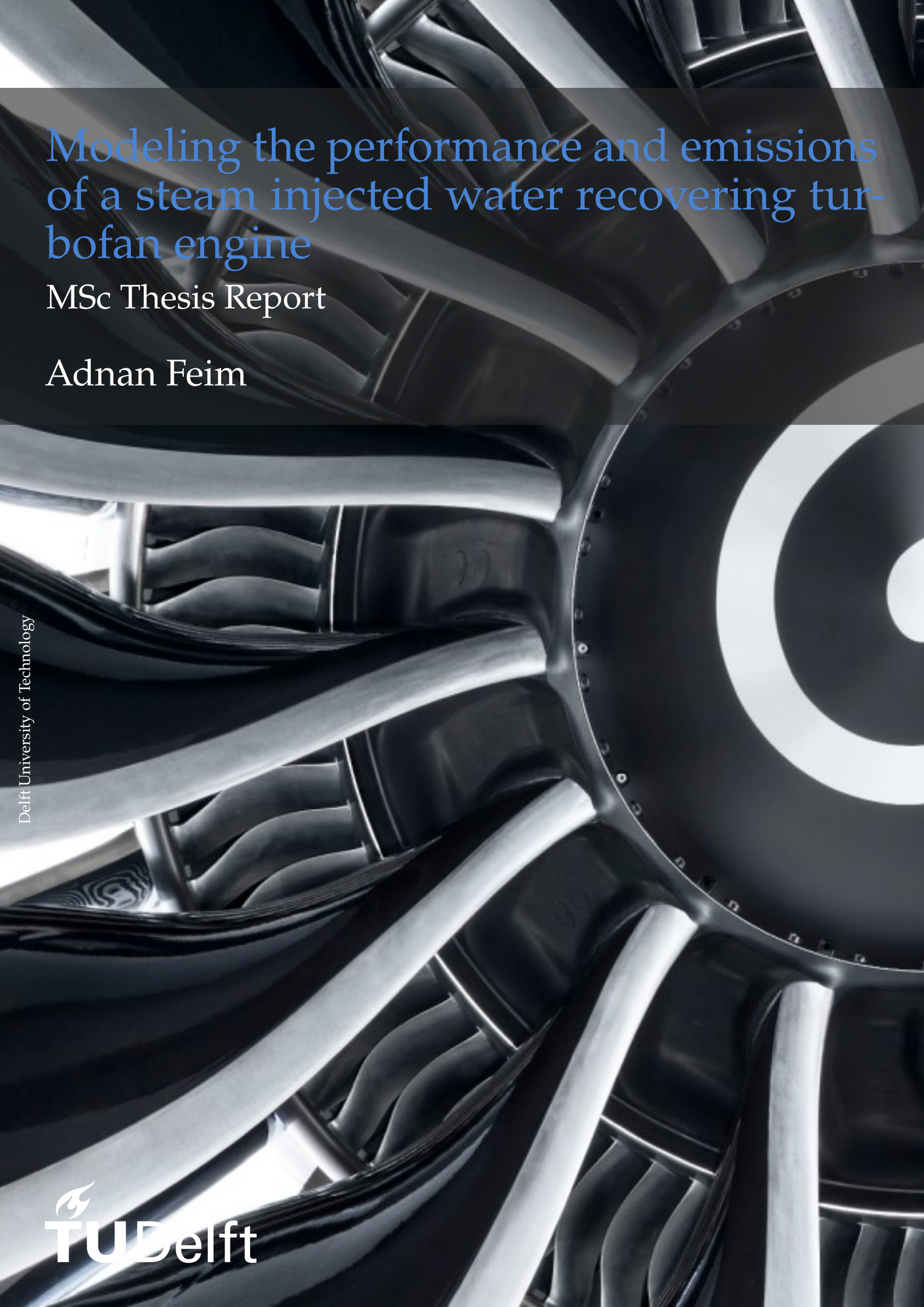

Delft University of Technology

TU Delft

Modeling the performance and emissions of a steam injected water recovering turbofan engine

MSc Thesis Report

by

Adnan Feim

to obtain the degree of Master of Science
at the Delft University of Technology,
to be defended publicly on 17 December 2025.

Student number:	4366336	
Project duration:	March 1, 2023 – 17 December 2025	
Thesis committee:	Prof. Anders Lundbladh,	GKN Aerospace, supervisor
	Prof. Arvind G. Rao,	TU Delft, supervisor
	Dr. Alexander Heidebrecht	TU Delft, additional
	Dr. Yinglu Tang	TU Delft, chair

Cover:	GE9X Engine by GE Aerospace
Style:	TU Delft Report Style

An electronic version of this thesis is available at `http://repository.tudelft.nl/`.

TU Delft

Abstract

The increase in air traffic creates the need for more efficient aircraft. Current design trends of increasing efficiency and reducing fuel consumption also lead to an increase in NOx emissions. Environmental considerations and regulations create a demand for aircraft engine technology with NOx emissions lower than that of current engines. The Steam Injected Water Recovering Turbofan engine is proposed; it injects steam before the combustion chamber and recovers it through condensation in a heat exchanger. Moreover, the cycle recovers more heat from the exhaust gasses, using them as a heat source in a Rankine cycle. The SIWRT was modeled in NPSS in collaboration with GKN Aerospace Sweden AB, to better understand this configuration. A new method was devised to model heat exchanger performance, referred to as a 'variable Cp NTU', capable of taking into account phase change. This new method was verified and partially validated. The engine was studied in a range of water to air of 1% to 7%. It was determined that it is capable of reducing thrust specific fuel consumption by up to 8% and NOx emissions by up to 66% compared to a conventional future turbofan. Increasing WAR leads to an increase in the fan bypass ratio (FBPR) mostly by reducing the core size. The SIWRT displays design trends similar to conventional turbofan when varying OPR, T_4, and FPR. At top of climb the condenser was not able to condense enough water for the engine to self sustain, thus extra water was supplied through an on board reservoir. The research questions were answered, and concluding remarks with suggestions for future work were provided.

Contents

List of Figures

List of Tables

Nomenclature

Symbols

Symbol	Definition	Unit
A	area	[m2]
C	stream capacity	W/K
C_p	isobaric heat capacity	J/kgK
C_v	isochoric heat capacity	J/kgK
H	total enthalpy	J
h	total specific enthalpy	J/kg
j	nested solver iteration	-
M	molar mass	g/mol
M_N	Mach number	-
$\dot{m}$	mass flow	kg/s
P	total pressure	Pa
p	partial pressure	Pa
q	mass fraction	-
R_{STM}	steam correction factor	-
T	total temperature	K
TF	technology factor	-
WAR	water/air ratio at combustor inlet	-
WFR	water/fuel ratio at combustor inlet	-
WGR	water/gas ratio (humidity)	-
x	vapor quality	-
γ	heat capacity ratio	[−]
ϵ	effectiveness	[−]
η	isentropic efficiency	[−]
ρ	density	$\left[\frac{kg}{m^3}\right]$

Abbreviations

Abbreviation	Definition
BP	bypass
BPR	bypass ratio
CBPR	condenser bypass ratio
DOC	direct operating cost
EI	emission index
FAR	fuel to air ratio
FBPR	fan bypass ratio
FPT	fluid property table
HPC	high pressure compressor
HPT	high pressure turbine
HRSG	heat recovery steam generator
LHV	lower heating value
LPC	low pressure compressor
LPT	low pressure turbine
MTO	maximum take-off
MTOW	maximum take-off weight
NPSS	Numerical Propulsion System Software
NTU	Number of transfer units
OPR	overall pressure ratio
PR	pressure ratio
REFPROP	Reference Fluid Thermodynamic and Transport Properties Database
SFC	(thrust) specific fuel consumption
SIWRT	steam injected water recovering turbofan
UHBPR	ultra high bypass ratio
V&V	verification and validation
WAR	water to air ratio
WET	Water Enhanced Turbofan
WGR	water to gas ratio

Subscripts

Subscripts describe location and/or processes.

Subscript	Definition
1,2	stream in heat HX
amb	ambient
comb	combustion
cond	condenser
des	on design
dg	dry gas
evap	evaporator
exh	exhaust
f	formation
g	gas
h	heat transfer
in	inlet
k	arbitrary specie
lat	latent
max	maximum
out	outlet
pmp	pump
ref	reference
s	sensible

Subscript	Definition
sat	saturation

Superscripts

Superscripts refer to composition and/or state.

Superscript	Definition
cond	condensed phase
dg	dry gas
g	(exhaust) gas
k	specie
sl	saturated liquid
sv	saturated vapor
vap	vapor phase
w	water

1

Introduction

Ever since the invention of the internal combustion engine, the increase in power and/or the reduction consumption have been at the forefront of innovation. A design parameter that lead to such improvement in turbofans has been the fan bypass ratio (BPR). By bypassing some of the air around the core where combustion happens and using it to generate thrust increases propulsive efficiency, leading to an increase in overall efficiency of the engine. As a result, over the years the design trends for turbofans has followed a continuous increase in BPR, as shown in figure 1.1.

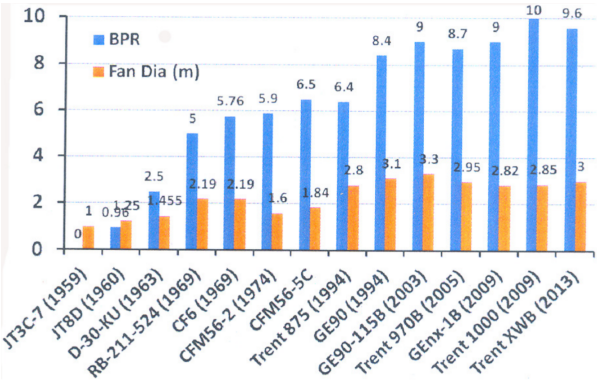

Figure 1.1: Bypass ratio and fan diameter of engines based on the year of certification [1].

Increase in BPR can be done by either increasing the fan size or reducing the core size. Either of those actions leads to diminishing returns as a comparatively smaller core is not able to power the fan. This drawback can be circumvented by increasing the overall pressure ratio (OPR) of the engine, which increases the power and efficiency of the core, allowing it to power a relatively larger fan. Therefore, the trends of increase in BPR have been in parallel with an increase in OPR, as seen in figure 1.2.

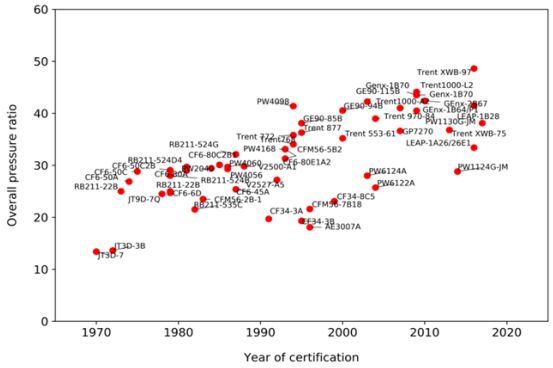

Figure 1.2: Variation of overall pressure ratio of engines versus their year of certification [2].

The benefit of higher OPR is an increased cycle efficiency at a given mass flow rate. At higher values, consumption is reduced and power is increased until is reaches a maximum. An increase beyond that

power is reduced. At very high OPR, the design can be constrained by the mechanical stress or thermal handling capabilities of components, for instance: turbine blades, combustor liner, compressor casing. If the engine is at the thermal limits, typically set by the turbine inlet temperature (TIT), a further increase in OPR is only possible if the amount of injected fuel is reduced. Therefore, finding an optimum is a careful balancing act between engine size, performance, and component life.

Same thermal limits apply to the combustor liner. This is why developments in materials and cooling technology have led to engines that can have a higher turbine inlet temperature, seen in figure 1.3. This allows the use of more fuel in the combustor, which allows more power to be generated for the same size engine. As a result the engine core can be downsized for the same thrust, reducing its weight and fuel consumption. For turbofans, higher TIT allows a smaller core to power a larger fan, which is beneficial for propulsive efficiency.

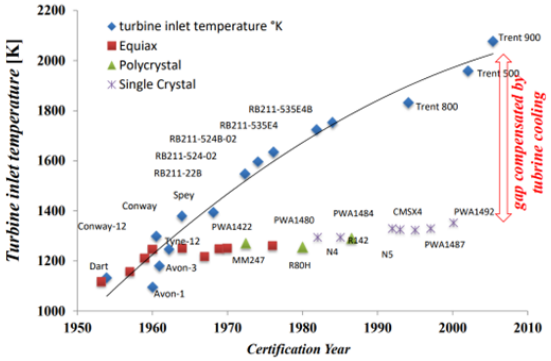

Figure 1.3: Turbine inlet temperature development over the years. [2]

The design trends have essentially lead to an increase in core thermal efficiency as well as BPR which is an increase in propulsive efficiency. This allows modern engines to power a bigger fan with a smaller core, seen in figure 1.4.

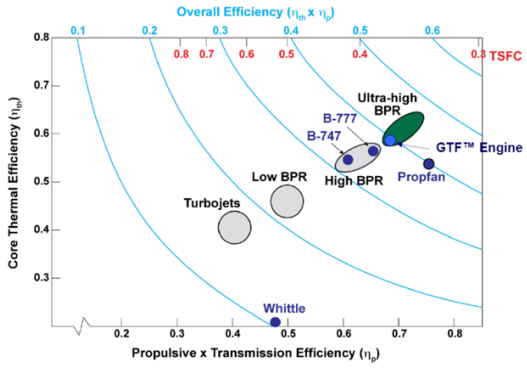

Figure 1.4: [3]

1.1. Motivation

Although current design limits are increasing efficiency, they are also reaching a point where improvements are only incremental. Moreover the higher combustor outlet temperatures lead to a substantial increase in NOx emissions. With the ever increasing air travel [4][5], it is impossible to ignore aviation's impact on the climate. Therefore an improvement in engine performance and emissions needs to come from the implementation of a new technology.

1.2. Research objective

The objective of this thesis is to create a simulation model of a Steam Injected Water Recovering Turbofan (SIWRT) engine for a long range aircraft and study its performance and emissions.

In order to complete the research objective, the following research questions are posed:

1.3. Research questions

1. What is the performance improvement of the steam-injected turbofan over a comparable conventional turbofan?
    - How does the thrust-specific fuel consumption change?
    - What are the relevant parameters that affect the performance of this engine?
2. How are emissions influenced by the implementation of such a cycle over the same mission?
    - What are the NO_x emissions?

1.4. Report outline

This report goes over the process of developing a performance simulation model of the SIWRT and studying the preliminary results. Chapter 2 sets the background for the SIWRT concept and background literature relevant to the topic. Chapter 3 describes the modeling software used and the reasons for the choice. Chapter 4 goes over the methodology steps for developing the model and sets new engine design parameters and the operating conditions. Chapter 5 is used for Verification and Validation of the relevant components of the model. Chapter 6 provides the results of this study and chapter 7 gives concluding remarks and suggestions for improvement of the model and pressing future work based on the results of this study.

2

Steam Injected Water Recovering Turbofan

2.1. Background

The steam injected water recovering turbofan (SIWRT) is a concept designed to increase thermal efficiency of engines while reducing NO_x emissions and contrails over a comparable conventional turbofan. Similar concept was developed in ground-based gas turbines, called the Cheng cycle [6]. There are several variations of the Cheng cycle [7], the one that the concept in this study is closest to is the "Cheng parallel dual-fluid cycle" [8] shown in Figure 2.1:

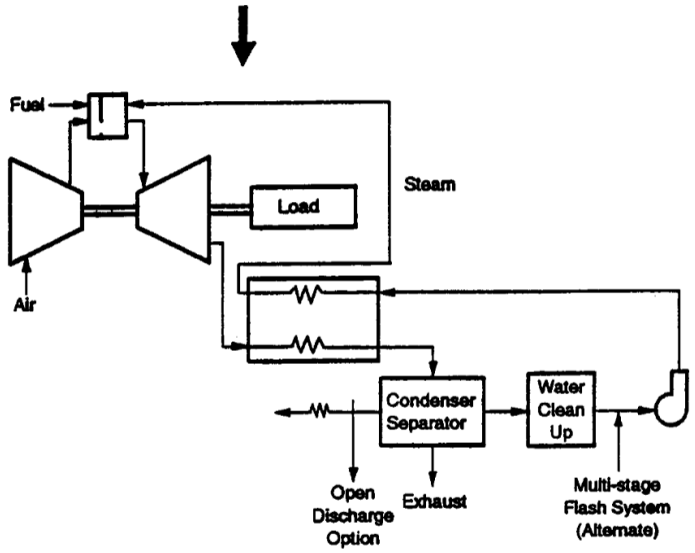

Figure 2.1: Cheng parallel dual-fluid cycle [8].

This cycle uses steam injection before combustion to humidify the air going into the combustor. The steam in created in a heat recovery steam generator (HRSG) which uses the heat from the waste exhaust gases to vaporize the water. The cooled exhaust gases go through a condenser / separator that separates liquid water from the humid exhaust gases which is fed into a water loop. The liquid water is then cleaned up before it is pumped to a sufficient pressure to go into the HRSG to be converted to steam before injection. This cycle has increased thermal efficiency, power density, and lowered NO_x emissions.

There is a lack of research on the Cheng cycle in the context of flying engines, with a notable exception of the recent studies performed by MTU Aero Engines on the Water Enhanced Turbofan (WET) concept [9] [10]. Their study concludes a possibility of a specific fuel consumption (SFC) reduction by 13%, reduced fuel burn and CO_2 by 10% over a conventional turbofan. Additionally, up to 90% reduction in NO_x and contrail reduction by more than 50% [11] [12].

In this study, the SIWRT is a similar concept to the WET Engine is investigated. The main difference is that the WET application is suited for a mid-range aircraft, while the SIWRT is sized for a long-range

aircraft application. A two-spool geared turbofan engine is adapted to implement the Cheng cycle. In the conventional turbofan engine the fan and low pressure compressor (LPC) are driven by the low pressure (LP) shaft , powered by the low pressure turbine (LPT). On the high pressure (HP) shaft, the high pressure compressor (HPC) is powered by a high pressure turbine (HPT). In the adapted engine, steam is injected right before the combustion chamber,resulting in combustion with humid air. The humid combustion products power the HPT and LPT after which the hot exhaust gases are used to heat an HRSG, which is here referred to as the evaporator. The now partly cooled exhaust is passed to a condenser which separates the water from the gases. Cooling the condenser is provided by part of the bypass air from the fan. The water is pressurized by a pump and sent to the evaporator and then in vaporized form to a steam turbine which helps power the LP shaft. The steam exiting the turbine is injected into the combustor to complete the water circuit. A simplified diagram of the system is given in Figure 2.2. A detailed diagram with all station numbers, bleeds, and ducts is given in Figure A.1.

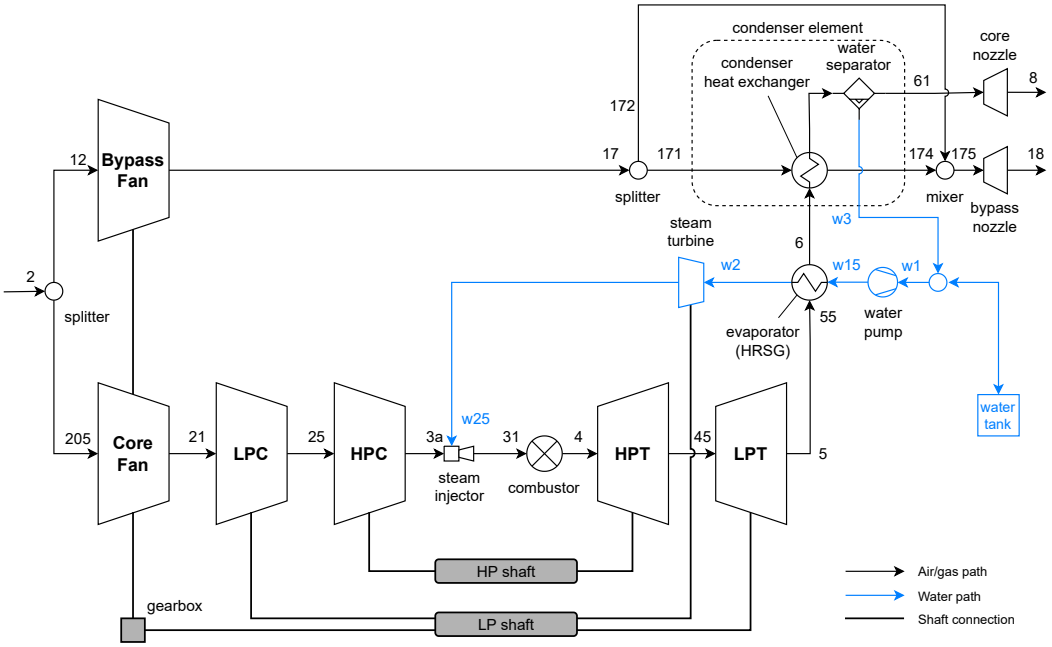

Figure 2.2: Process flow diagram of the Steam injected water recovering turbofan (SIWRT) diagram with station notation. Bleeds are not shown.

2.2. Humid combustion

Humid air slows the combustion reaction time and reduces flame temperature temperature for a given fuel-to-air ratio (FAR). The higher mass flow, due to addition of steam, allows for more work to be extracted by the turbines, provided enough fuel is added to raise the gases to the same temperature as for the conventional engine. Since the compressor flow is not increased, the net power (turbine minus compressor power) is increased and the thermodynamic efficiency of the cycle also increases.

The addition of water vapor in the combustor reduces the stoichiometric flame temperature for a given equivalence ratio. Since most of the NOx is generated in very hot, near stoichiometric flame zone, this leads to a reduction in NO_x emissions, shown in Figure 2.3a. If the flame temperature is kept same as in dry combustion, NOx is still lowered in the presence of humidity. however, the same conditions lead to an increase in CO emissions [13][14].

2.3. Heat / water recovery

The exhaust gases expelled from the core of a conventional turbofan contain heat that can potentially be utilized to increase its thrust. In the SIWRT, heat is recovered through the evaporator to be fed back into the engine, increasing its thermal efficiency. Additionally, the condenser transfers heat into part of the bypass flow, which may provide a thrust increase by the use of the Meredith effect [16].

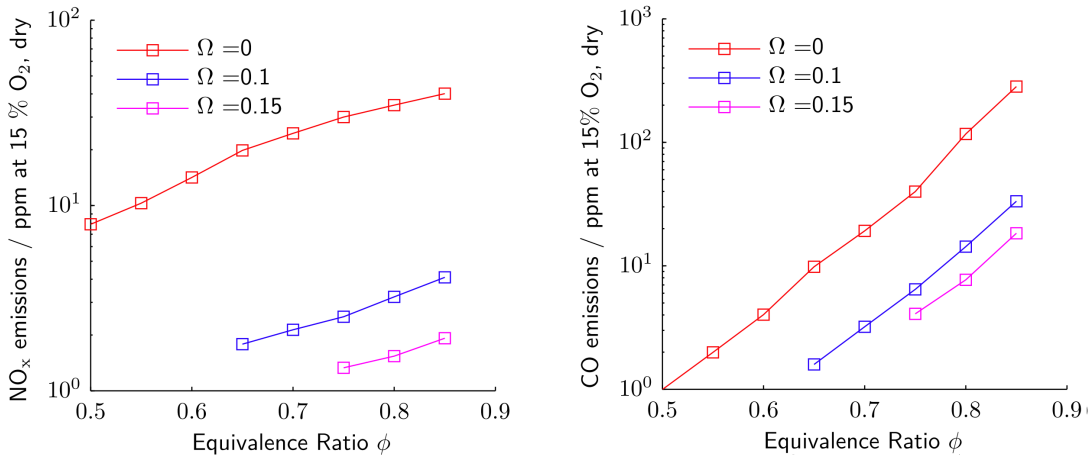

(a) Evaporator effectiveness vs fan bypass ratio for different overall pressure ratio and WAR values.

(b) Evaporator total heat transfer rate vs fan bypass ratio for different overall pressure and WAR values.

Figure 2.3: Experimental results for NOx and CO emissions versus equivalence ratio for dry and humid Kerosene combustion[15].

2.4. Rankine cycle

The water pump, evaporator, and steam turbine contained in the water loop constitute an open Rankine cycle. The excess power generated by that cycle is fed into the LP shaft. Increasing the pressure rise in the pump allows for more power to be extracted by the steam turbine. At higher pressures the latent heat of vaporization of water is lower, thus less heat is required for complete the phase change. However, at higher pressure the boiling temperature of water is increased, increasing the heat needed to reach boiling and reducing the amount of heat transfer in the evaporator. In order to maximize the work recovered by the Rankine cycle, the pump pressure rise must be optimized in relation to the temperature of the hot exhaust gases heating the evaporator.

3

Numerical Propulsion System Simulation

Numerical Propulsion System Simulation (NPSS) is a an advanced component-based, object-oriented, non-linear thermodynamic modeling environment dedicated for thermodynamic cycles. It is used by the aerospace industry for modeling of turbomachinery, air-breathing propulsion systems, liquid rocket engines, engine control systems, and system model integration. It can also be used for modeling of refrigeration cycles, multi-phase heat transfer systems, or emissions analyses [17]. It uses a specific interpreted language, based on C++[18][19].

An NPSS engine model is assembled from a collection of interconnected components, called elements. Elements contain ports (fluid, fuel, shaft) that are used as data input or output. Data between element ports is transferred using links. For the purposes of this report, however, they shall be referred to as components.

Performance can be calculated in one of two conditions: design or off-design. The first run needs to be a design as that is used to size the engine (ducts, turbomachinery, nozzles, etc.), which is also referred to as a rubber engine [20]. Multiple design runs with different conditions result in different engines. The off-design runs are used if the performance of the same engine in a different condition is of interest. Typically one design is run that sizes the engine and subsequently off-design runs study the performance at varying conditions. All components in NPSS have design and off-design modes that may use different sets of variables in its calculations[18].

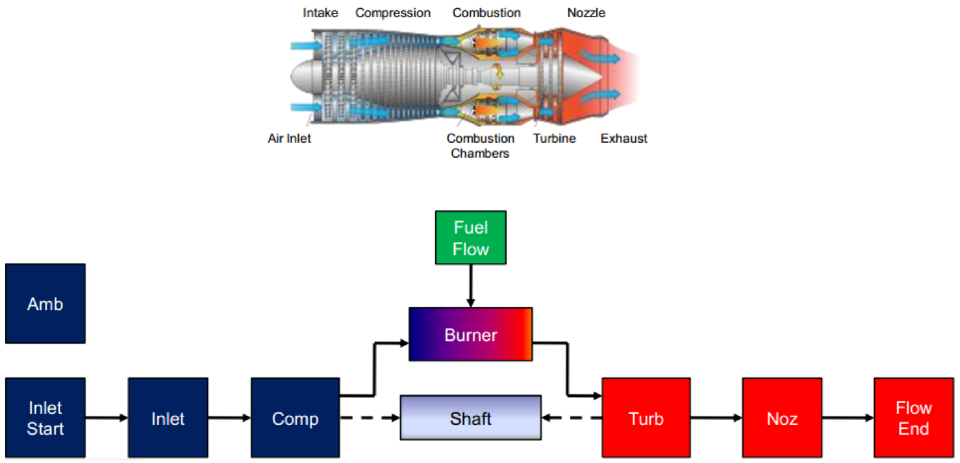

Figure 3.1: Example NPSS model of a turbojet [21][22].

3.1. Component modeling

NPSS provides a library of components that can be used to create basic systems. A few of these components are: compressor, turbine, burner, heat exchanger, duct, splitter, mixer, etc. Many components contain a switch for 'design' and 'off-design' which changes the way the components determines the output.

3.1.1. Compressor

Compressors have two inputs: flow in and shaft in and a single flow out output. The user sets the design parameters for pressure ratio (PR), isentropic efficiency, and/or corrected mass flow. These values are used in the design runs and additionally are used to size the compressor using unscaled compressor maps. Once the map is scaled, the scaled map can be used for off-design runs [18].

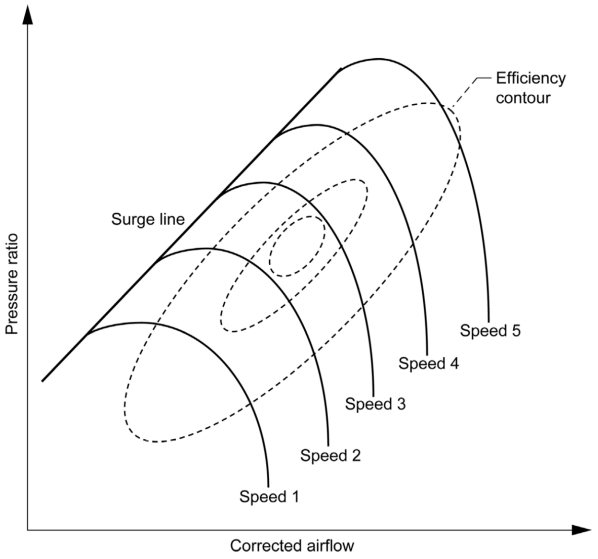

Figure 3.2: Example unscaled compressor map[18].

3.1.2. Burner

The burner component has an inlet for air flow and one for fuel flow. It uses them for combustion, which results in a temperature rise. The hot exhaust gases are expelled through the outlet. The burner works in three modes: temperature, fuel flow, or fuel-to-air ratio (FAR) [18].

- Temperature: user sets the required burner outlet temperature and the solver calculates the required fuel flow and provides the resulting FAR.
- Fuel flow: user sets the fuel mass flow and the solver calculates the outlet temperature and FAR that would result in the given conditions.
- Fuel-to-air: user sets the required FAR and the solver calculates the amount of fuel that is needed and the resulting outlet temperature.

3.1.3. Heat Exchanger

The heat exchanger component provided by the NPSS library is a dual-fluid heat exchanger with two fluid inputs and two fluid outputs. It uses either effectiveness or heat transfer rate to determine outlet conditions and assumes constant Cp for each fluid taken as the inlet Cp value.

3.1.4. Performance - NOx emissions

NPSS uses a performance component that can be used to perform various calculations. The one used at GKN Aerospace was modified internally to calculate NOx emissions using a correlation on combustor inlet pressure and temperature (P3, T3). The author had no access to the methodology or the data of how it works, which is why other methods are introduced in this study.

3.1.5. Custom components

In NPSS users are able to modify the source code on each of the components to create custom versions of existing components or entirely new ones. This includes the use of many of the software's functionalities, allowing for the application of very specific functions. Additionally, nested solvers can be used inside components

3.1.6. Linking components

Different components can be linked using a variety of link ports that are used to transfer different types of data:

- fluid - used for any fluid ports (air, exhaust gas, water). Defined in a given direction and fluid is not allowed to flow in the opposite direction.
- fuel - used for any fuel ports. Typically used between a fuel start and burner.
- shaft - used for any rotating shafts to transfer work.
- data - used for any data that can be transferred between components without a physical connection.
- file - used to transfer data from a file into an component (i.e. compressor maps)

3.2. Thermodynamic package

NPSS employs the use of several thermodynamic databases that are called "thermopackages" to estimate the properties of fluids at flow stations. Each flow station is defined as a particular thermopackage. The conditions of that flow station determines fluid properties such as: total temperature, enthalpy, entropy, pressure, and specific heat [23]. Detailed information on species and their properties in the thermopackage is given in Appendix C. The thermopackages used in the model are "Janaf" and "FPT". Janaf is used for all gas mixtures, while FPT is used for all pure water fluid ports.

3.2.1. Janaf

The Janaf thermopackage is a chemical model based on NASA's Chemical Equilibrium Application (CEA). With the main difference being that Janaf uses a limited number of species that are typically seen in hydrocarbon combustion. This makes Janaf calculations significantly faster than CEA. The enthalpy of species in Janaf is defined as:

$$h(T, P) = h_s(T, P) + h_l(P) + h_f \tag{3.1}$$

Where h as a function of temperature and pressure is the total specific enthalpy, h_s is the sensible enthalpy, h_l is the latent enthalpy of phase change, and h_f is the enthalpy of formation. The species present with their heat of formation are given in Appendix C. The sensible enthalpy is zero at reference temperature and pressure:

$$h_s(T_{ref}, P_{ref}) = 0 \qquad \frac{\text{J}}{\text{kgK}} \tag{3.2}$$

$$T_{ref} = 298.15 \qquad \text{K} \tag{3.3}$$

$$P_{ref} = 101325 \qquad \text{Pa} \tag{3.4}$$

Gas mixtures

Janaf provides mixture species mass fraction and allows the user to set a custom mixture. The default dry and humid air mixtures are shown in Appendix C.

3.2.2. FPT - Water

It is possible to set custom fluid property tables in NPSS. By generating fluid property data for water in REFPROP and converting them to a format that can be read by NPSS, the water properties can be used in the model. Using the same reference definition as the Janaf thermopackage from Eq. 3.1, allows for the FPT to be used directly with Janaf without the need of any conversion. The pressure-enthalpy diagram of the water generated data from REFPROP, is given in Figure 3.3 and the water saturation line is given in 3.4

Using two inputs from temperature, pressure, enthalpy, and entropy, the water state is determined and water properties are output: density, isochoric heat capacity, isobaric heat capacity, heat capacity ratio.

The water state is determined by using input from two parameters: temperature, pressure, enthalpy, or entropy. The water properties that can be used as an output are: density, isochoric heat capacity, isobaric heat capacity, heat capacity ratio.

3.3. Solver

NPSS employs a global solver that uses the Newton-Raphson method that is able to provide solutions for constrained systems [24]. The solver has a set of dependent and independent pairs. The dependents are variables that the solver varies under user set starting condition and parameters. The independents are equations that the solver attempts to match both sides of [18]. The user is able to set the order of

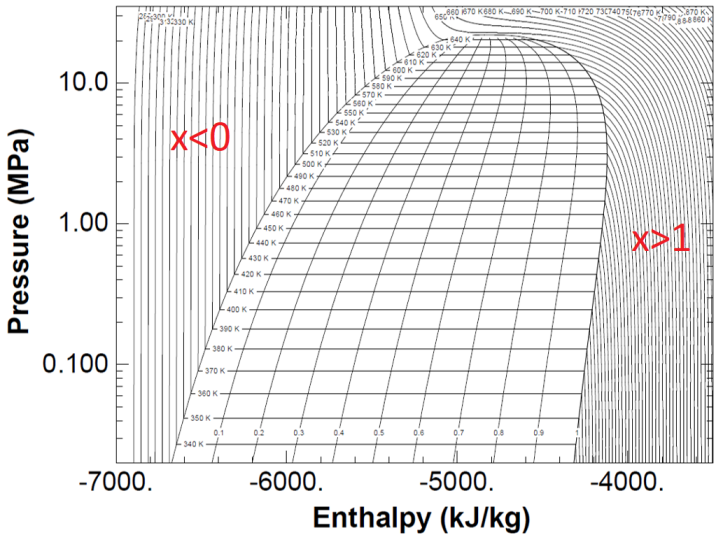

Figure 3.3: Water P-h diagram data from REFPROP with isotherms, saturation curves, and iso-quality curves in dual phase region.

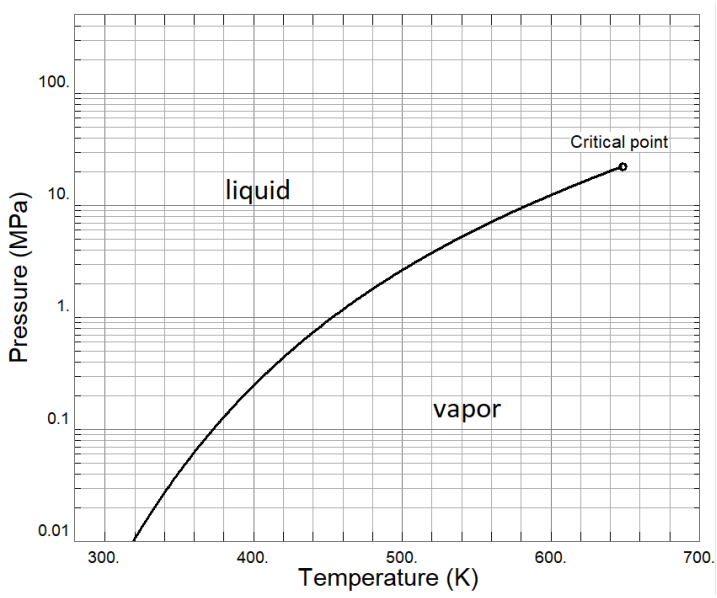

Figure 3.4: Water saturation line and critical point.

calculation of components and if any component contains a solver within, the global solver waits for that component's solver to complete its iteration before continuing with the next.

The solver converges when the solution of each independent equation is within tolerance and all nested solvers have converged. Each iteration uses the values of parameters that resulted from the previous iteration and has no ability to distinguish when a value is outside of given bounds. This can lead to a parameter value reaching infinity and after a non-converged run that value is fed into the next iteration, ensuring that every subsequent run is not converged. The user needs to take great care in preventing that from happening, or identify which variables contain that risk and reset their initial conditions.

4

Methodology

This chapter goes over the methodology used in the modeling of the SIWRT engine. It goes over the key components that characterize the cycle: water injector, evaporator, condenser, water pump, NOx emissions and the complete model.

4.1. Water Injection

Water injection before the combustor mixes the incoming water vapor with the core air flow. Because the injected water amount is relatively small, the resulting humid air is assumed to have the same pressure as the incoming core flow. The mass and energy balance is given by:

$$\dot{m}_{31} = \dot{m}_3 + \dot{m}_{w025} \tag{4.1}$$

$$\dot{m}_{31} h_{31} = \dot{m}_3 h_3 + \dot{m}_{w025} h_{w025} \tag{4.2}$$

Where $\dot{m}_{31}$ is the mass flow after steam injection, $\dot{m}_3$ is the mass flow before steam injection and after all bleed ports, $\dot{m}_{w25}$ is the mass flow of the water to be injected, while h is the specific enthalpy of the flow in the respective station. An important parameter in this engine is the water content in the air. Following the notation from NPSS, it is given as water to air ratio (WAR) and is defined as the mass fraction of the water to dry air:

$$WAR = \frac{\dot{m}_{w25}}{\dot{m}_3} \tag{4.3}$$

Equation 4.3 only holds for the assumption that the engine is ingesting dry air. For humid ambient conditions, this would need to be reworked.

4.2. Evaporator

The evaporator model is a modified NPSS heat exchanger component that can use different thermopackages for the two streams. It can take as input the heat transfer rate or an effectiveness. Because the heat capacity and enthalpy of the water stream varies significantly with temperature and pressure, a modified definition of effectiveness needs to be used: this includes the mean total change in enthalpy, which takes into account the different heat capacities between liquid and vapor as well as latent heat of vaporization. The model applies a fixed pressure drop before any enthalpy calculations.

4.2.1. Effectiveness

Heat exchanger effectiveness is defined as the ratio between rate of heat transfer and the maximum rate of heat transfer [25].

$$\epsilon = \frac{\dot{Q}}{\dot{Q}_{max}} \tag{4.4}$$

Where ϵ is the heat exchanger effectiveness, $\dot{Q}$ is the heat transfer rate, and $\dot{Q}_{max}$ is the highest possible heat transfer rate between the two streams. $\dot{Q}_{max}$ is determined by the stream that has the lower stream capacity when reaching the other stream's inlet temperature. In this heat exchanger, stream 1 is defined as the exhaust gas, while stream 2 is the water flow.

$$C_1 = \dot{m}_1 \overline{Cp}_1 = \dot{m}_1 \frac{h_1(T_5) - h_1(T_{w15})}{T_5 - T_{w15}} \tag{4.5}$$

$$C_2 = \dot{m}_2 \overline{Cp}_2 = \dot{m}_2 \frac{h_2(T_{w15}, P_{w2}) - h_2(T_5, P_{w2})}{T_{w15} - T_5} \tag{4.6}$$

Where C is the stream capacity of the given stream, $\overline{Cp}$ is the mean heat capacity of the given stream, h is the total specific enthalpy of the given stream, and T is the total temperature of the given stream and port, and P is the total pressure of the given stream and port. The maximum rate of heat transfer is therefore given by:

$$\dot{Q}_{max} = (C_1, C_2)_{min}(T_{w15} - T_5) \tag{4.7}$$

4.2.2. Vapor quality

When the water undergoes a phase change from liquid to vapor, the latent heat required can be multiple times more than the heating required from room temperature to right before boiling, as shown in Figure 4.1.

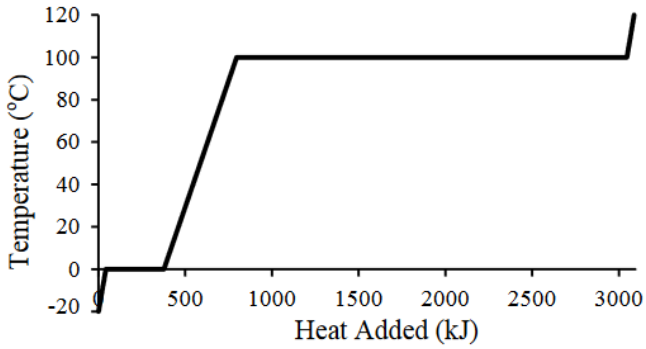

Figure 4.1: Temperature profile for phase change from subcooled ice to superheated steam [26] at 1atm.

Vapor quality is a useful parameter often used in dual-phase flows. Since temperature during phase-change remains mostly constant, the vapor quality is an indicator for how much of the heat of evaporation was transferred. To ensure that the steam in the turbine is dry, i.e. free from droplets, the enthalpy needs to be significantly higher than the enthalpy of saturated vapor. Normally, the temperature drop in the turbine moves the vapor closer to condensation[1]. Despite the reduced pressure the steam quality drops. Thus the most critical point is the steam turbine outlet. A suitable margin to formation of drops due to inhomogeneous temperature in the flow can be defined by setting a minimum vapor quality above 1.

$$x = \frac{h^w - h^{w,sl}}{h^{w,sv} - h^{w,sl}} \tag{4.8}$$

Where x is the vapor quality, h^w is the water enthalpy and $h^{w,sl}$ is the saturated liquid enthalpy of water at the given pressure, and $h^{w,sv}$ is the saturated vapor enthalpy of water at a given pressure. A vapor quality $x = 0$ means that the water is at the liquid saturation line, $x = 1$ means the water is at the vapor saturation line. In most applications, vapor quality values outside the range of 0 to 1 are not useful. However, values outside the range $0 \leq x \leq 1$ are still useful in the model as they can be used as constraints to ensure the required conditions are achieved. Additionally, they provide mathematical solution continuity which helps the solver converge and stability. Negative values means that water is liquid and the number is the ratio of the required specific enthalpy needed to reach saturation to the latent enthalpy at that pressure. On the other hand, values above 1 show where water is a vapor with the number being the ratio between the specific enthalpy above the saturated vapor curve to the latent enthalpy at that pressure.

[1]This would not be true of the steam turbine efficiency is very low. In that case the pressure drops with little enthalpy drop.

4.3. Condenser

The condenser is a heat exchanger that is designed to cool a fluid until it undergoes a phase change from vapor to liquid. Most condenser application are in a Rankine Cycle engines that use water as a working fluid but other applications make use of different working fluids, such as heat pump, refrigerant, and Organic Rankine Cycles [27]. What these application have in common is the use of a single species fluid that enters the condenser as a superheated vapor and is cooled until it reaches a subcooled liquid state at the outlet.

The SIWRT's condenser is different, as the goal is to cool a gas mixture and have only one species (water) condense to a liquid state. This is possible because the temperature at which water can exist in liquid state is much higher than the that of the remaining species contained in the gas: N_2, O_2, CO_2, CO, NO_x. Therefore as the gas mixture temperature is reduced, water condenses much earlier, which makes the fluid inside and after the condenser a gas mixture with liquid water. It is assumed that all of the condensed water is separated and fed back into the cycle.

Other names for such a device are 'dryer' or 'dehumidifier', but in this study it shall be referred to as a condenser. The component in this model is a modified heat exchanger, which uses 0-D lumped parameter heat transfer and flow humidity calculations. As a result it determines how much of the incoming water is converted to liquid.

The cooling flow of the condenser uses part of the bypass flow, therefore a new parameter is introduced: condenser bypass ratio (CBPR) which is defined as:

$$CBPR = \frac{\dot{m}_{172}}{\dot{m}_{171}} \tag{4.9}$$

Humidity

In order to determine condensation properties, humidity calculations are required. Using the composition of the gas, provided by NPSS, the water to gas ratio is determined. The water gas ratio is defined as the mass ratio between water and remaining species in the mixture (dry gas). Water to gas ratio is given by:

$$WGR = \frac{q^w}{1 - q^w} \tag{4.10}$$

Where WGR is the water gas ratio and q^w is the water mass fraction in the mixture. If the gas is air, then the definition leads to $WGR = WAR$.

Saturation humidity

At given conditions (temperature and pressure), when a gas is not able to hold any more water vapor it has reached its saturation humidity. At this point the water vapor is in equilibrium with liquid water. Any additional water remains in liquid state. Under these conditions the partial pressure of pure water is equal to the partial pressure of vapor water in the mixture. Saturation humidity is given by [28]:

$$WGR^{sat} = \frac{M^w}{M^{dg}} \frac{p^{w,sat}}{P - p^{w,sat}} \tag{4.11}$$

Where WGR^{sat} is the saturation humidity (mass ratio), M^w is the water molar mass, M^{dg} is the dry gas molar mass, $p^{w,sat}$ is the saturation pressure of water, and P is the mixture pressure. The dry gas molar mass is determined by the average molar mass of mixtures:

$$\frac{\mathbf{1}}{\overline{\mathbf{M}}} = \sum_{\mathbf{k}} \frac{\mathbf{q^k}}{\mathbf{M^k}} \tag{4.12}$$

Where $\overline{\mathbf{M}}$ is the average molar mass of an arbitrary mixture, $\mathbf{k}$ designates the species, given in table C.1, that are contained in the mixture. If the mixture is split into water and dry gas, equation 4.12 leads to:

$$\frac{1}{M^g} = \frac{q^w}{M^w} + \frac{1 - q^w}{M^{dg}} \tag{4.13}$$

Where M^g is the molar mass of the humid gas mixture. The dry gas molar mass is given by:

$$M^{dg} = \frac{1 - q^w}{\frac{1}{M^g} - \frac{q^w}{M^w}} \tag{4.14}$$

Pressure
Using the input for pressure drop in each stream, the outlet pressures are determined:

$$P_{174} = P_{171} - dP_1 \tag{4.15}$$
$$P_7 = P_6 - dP_2 \tag{4.16}$$
$$P_{w1} = P_7 \tag{4.17}$$

Where P_{174}, P_{171} are the stream 1 outlet and inlet total pressures, respectively. P_7, P_6 are the stream 2 outlet and inlet total pressures, respectively. While dP_1 and dP_2 are the total pressure drops of stream 1 and 2 respectively and P_{w1} is the condensed water pressure.

Mass
Conservation of mass is given by:

$$\dot{m}_{171} = \dot{m}_{174} \tag{4.18}$$
$$\dot{m}_6 = \dot{m}_7 + \dot{m}_{w1} \tag{4.19}$$

Where $\dot{m}_{171}$ and $\dot{m}_{174}$ are stream 1 inlet and outlet mass flows, respectively; $\dot{m}_6$ and $\dot{m}_7$ are stream 2 inlet and outlet mass flows, respectively. Stream 3, is the liquid water which only has an outlet, given by $\dot{m}_{w1}$. The gaseous flow of stream 2 can be split into dry gas and water vapor:

$$\dot{m}_6 = \dot{m}_6^{dg} + \dot{m}_6^{w,vap} \tag{4.20}$$
$$\dot{m}_7 = \dot{m}_7^{dg} + \dot{m}_7^{w,vap} \tag{4.21}$$
$$\dot{m}_6^{dg} = \dot{m}_7^{dg} = \dot{m}_2^{dg} \tag{4.22}$$

Where $\dot{m}_6^{dg}$ and $\dot{m}_6^{w,vap}$ are the stream 2 inlet dry gas and water vapor mass flows, respectively, while $\dot{m}_7^{dg}$ and $\dot{m}_7^{w,vap}$ are the stream 2 outlet dry gas and water vapor mass flows, respectively and $\dot{m}_2^{dg}$ is the dry gas mass flow of stream 2, which remains unchanged between inlet and outlet.

At a given outlet temperature of stream 2, the outlet saturation humidity is checked against the inlet absolute humidity. If $WGR_6 \leq WGR_7^{sat}$, then no condensation occurs and the composition of the mixture remains unchanged, therefore:

$$WGR_7 = WGR_6 \tag{4.23}$$
$$\dot{m}_{w1} = 0 \tag{4.24}$$

If $WGR_6 > WGR_7^{sat}$ the amount of water vapor in the mixture is greater than what the mixture under the conditions can hold as vapor, condensation occurs. The maximum amount of water that can be condensed is at saturation humidity, thus:

$$\dot{m}_7^{w,vap} = \dot{m}_2^{dg} \cdot WGR_7^{sat} \tag{4.25}$$
$$\dot{m}_{w1} = \dot{m}_6^{w,vap} - \dot{m}_7^{w,vap} \tag{4.26}$$
$$q_7^w = \frac{\dot{m}_7^{w,vap}}{\dot{m}_2^{dg} + \dot{m}_7^{w,vap}} \tag{4.27}$$

Where $\dot{m}_{w1}$ is the flow of water in the condensed phase. Adjusting the mass fraction of the remaining species in the gas mixture:

$$q_7^k = \frac{\dot{m}_2^{dg} + \dot{m}_6^{w,vap}}{\dot{m}_2^{dg} + \dot{m}_7^{w,vap}} q_6^k \tag{4.28}$$

Enthalpy
The energy balance of streams 1, 2, and 3 are given by the rate of change in enthalpy within the control volume:

$$\dot{H}_{174} = \dot{H}_{171} - \dot{Q} \tag{4.29}$$
$$\dot{H}_7 + \dot{H}_{w1} = \dot{H}_6 + \dot{Q} \tag{4.30}$$

Here $\dot{H}$ is the rate of enthalpy change and $\dot{Q}$ is the heat transfer rate of the heat exchanger. NPSS defines the heat transfer rate in heat exchangers as positive when heat is transferred from stream 1 to stream 2. The gas model provides the specific enthalpy of each stream, therefore the heat transfer rate in streams 2 and 3 can be calculated:

$$\dot{Q} = \dot{H}_7 + \dot{H}_{w1} - \dot{H}_6 \tag{4.31}$$
$$\dot{Q} = \dot{m}_7 h_7 + \dot{m}_3 h_3 - \dot{m}_6 h_6 \tag{4.32}$$

The heat transfer of stream 1 follows:

$$\dot{m}_{174} h_{174} = \dot{m}_{171} h_{171} - \dot{Q} \tag{4.33}$$

4.4. NTU method

In Sections 4.2 and 4.3 the methods for determining the outlet conditions for given heat exchanger performance are outlined. In order to determine what that performance is, additional methods are required. The goal is to determine the outlet conditions of both streams with only the inlet conditions and a few design parameters. For this, a modified NTU method is chosen.

The standard NTU (Number of transfer units) method uses the inlet conditions to determine the heat exchanger effectiveness:

$$C = C_p \dot{m} \tag{4.34}$$
$$R = \frac{min(C_1, C_2)}{max(C_1, C_2)} \tag{4.35}$$
$$NTU = \frac{U A_h}{min(C_1, C_2)} \tag{4.36}$$
$$\varepsilon_{NTU} = f(NTU, R) \tag{4.37}$$

Where C is the stream capacity, R is the stream capacity ratio, subscripts 1 and 2 designate each fluid stream, U is the overall heat transfer coefficient, A_h is the heat transfer area, and ε_{NTU} is the effectiveness resulting from the NTU method. Effectiveness is a function of NTU and R where the equation is determined from literature based on the type of heat exchanger (counter-flow, cross-flow, etc.). For this model a counter-flow configuration is chosen [25]. In reality, the best configuration is likely a multi-pass cross-flow with tens of passes, however, for the NTU method that corresponds to a counter-flow heat exchanger [29].

$$\varepsilon = \frac{1 - e^{(R-1)NTU}}{1 - Re^{(R-1)NTU}} \tag{4.38}$$

The limitation of the classic NTU approach is the use of a constant C_p seen in Equation 4.34. In this study, both heat exchangers employ phase change, which leads to large variations in specific heat. Because of these variations, constant C_p is not a valid assumption, which is why, a mean heat capacity is used:

$$\overline{Cp} = \frac{h_o - h_i}{T_o - T_i} \tag{4.39}$$

Where $\overline{Cp}$ is the mean specific heat, h_o and h_i are the outlet and inlet enthalpies, respectively. T_o and T_i are the outlet and inlet temperatures. In this approach the outlet conditions are determined by $\overline{Cp}$, but $\overline{Cp}$ is determined by the outlet conditions. In order to find a solution a nested solver was created in both evaporator and condenser that iterates a solution. Figure 4.2 shows a single iteration loop, j: a guess is made for the outlet temperature or enthalpy, this allows the determination of the total heat transfer rate. Knowing the maximum possible heat transfer rate and the total heat transfer rate, an

effectiveness is determined as per definition. In parallel, the guess for outlet conditions allows for the stream capacity C from $\overline{Cp}$, which is used to determine NTU and the effectiveness as a result of the NTU method ε_{NTU}. The effectiveness error is given by the difference between the two effectiveness results:

$$\varepsilon_{err} = \varepsilon - \varepsilon_{NTU} \tag{4.40}$$

If the error is zero within tolerance, the loops is ended and this is the solution. If not, another iteration is started with another guess.

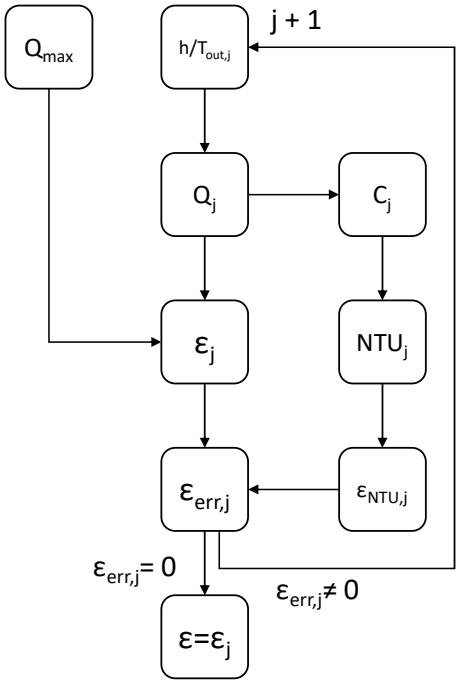

Figure 4.2: Variable C_p NTU approach solver order of operation and iteration loop. A guess is made for the outlet conditions $(h/T_{out,j})$, which results in a heat transfer rate Q_j. The maximum possible heat transfer rate Q_{max} is determined, leading to calculating the effectiveness ε. In parallel from Q_j, the NTU method is used to calculate effectiveness: $\varepsilon_{NTU,j}$. The two effectiveness values are compared, if they are within tolerance of each other, the solution is found. If not, another iteration is created with a new initial guess for outlet conditions.

4.5. Water Pump

Water pump component was added for a separate library[21] that works similarly to an NPSS compressor component, with the main difference being that the maps are different. It was slightly modified to take pressure rise as input. On design, the pump parameters are given by:

$$P_{w15} = P_{w1} + dP_{des} \tag{4.41}$$

$$PR_{pmp} = \frac{P_{w15}}{P_{w1}} \tag{4.42}$$

Where P_{w15} is the pump outlet total pressure, P_{w1} is the pump inlet total pressure, dP_{des} is the pump pressure rise on design and PR_{pmp} is the pump pressure ratio. The design point sizes the pump maps shown in Fig. 4.3 and the off-design point is determined by:

$$PR_{pmp} = \text{Head}\frac{\rho_{w1}}{P_{w1}}g \tag{4.43}$$

Where ρ_{w1} is the pump inlet density and g is gravitational acceleration.

4.6. Emissions

This section goes over the emissions, correlating NOx emissions with engine parameters as well as steam injection. A qualitative description is given of how contrails and CO/UHC emissions are expected to change.

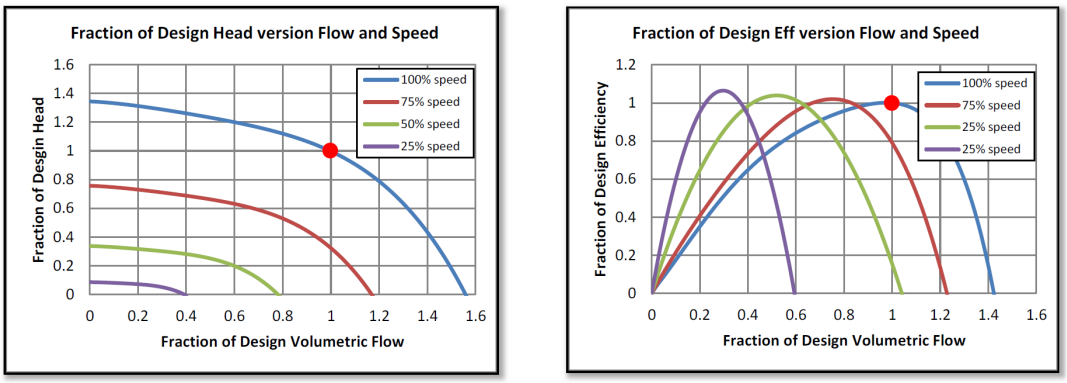

Figure 4.3: Water pump maps. Red point designates the design point.

4.6.1. NO_x emissions

Determining NO_x emissions is a process based on correlations from the literature. Although NPSS provides a component that estimates the emission index for NO_x ($EINO_x$), it was determined that it is a correlation that does not take into account combustion humidity. Kaiser et al. [11] provide a detailed overview of a variety of NO_x correlations. One of these methods is from NASA empirical NOx severity factor that takes combustor inlet temperature and pressure[30]:

$$S_{NO_x} = \left(\frac{P_{31}}{2.965 \cdot 10^6}\right)^{0.4} \cdot \exp\left(\frac{T_{31} - 826}{194}\right) \tag{4.44}$$

Where P_{31} and T_{31} are the total pressure and temperature of the combustor inlet, respectively. The effect of humidity in ambient air is neglected because it is assumed that the ambient air is dry. The total $EINO_x$ is given by:

$$EINO_x = 32 \cdot S_{NO_x} \cdot TF \cdot R_{STM} \tag{4.45}$$

Where TF is a technology factor and R_{STM} is a steam correction factor. These two values characterize the two methods that are considered for determining $EINO_x$:

GasTurb

The method used by GasTurb [31] does not take into account the technology factor, therefore $TF = 1$. However, for humid combustion, the steam correction factor is provided by Hung W.S.Y. [32]:

$$R_{STM,GasTurb} = \exp - (0.2\text{WFR}^2 + 1.41\text{WFR}) \tag{4.46}$$

Where WFR is the water/fuel mass ratio at the combustor inlet.

MTU

For the WET engine by MTU, Kaiser S. [11] use a technology factor $TF = 0.72$ and a steam correction factor derived by data from Schimek S. [15]:

$$R_{STM,MTU} = \exp\left(\frac{-2.465\text{WAR}^2 - 0.915\text{WAR}}{\text{WAR}^2 + 0.0516}\right) \tag{4.47}$$

4.6.2. Contrails

Condensation trails, among other pollutants, contribute to the greenhouse effect by trapping radiation rays and leads to a net warming of the surface [33]. In simple terms, contrails are condensation clouds formed by the crystallization of the water contained in the exhaust gases of engines. Factors that contribute to the formation of contrails are as follows:

- High water content leads to an increase in water that can condense and freeze to form cirrus clouds.
- Particulate emissions can also be a catalyst for the formation of ice crystals. In general, a large number of particulates leads to more surface area for water to freeze, thus leading to more contrails.

In the SIWRT concept at this stage is unclear if all or more of the injected water as steam can be recovered after condensing. Although recovering all or more water is key for the correct operation of the system during a complete mission which would lead to a reduction in water emissions expelled through the nozzle. Additionally, the water capturing mechanism is likely to capture any solid particles, which should reduce the particulate emissions, leading to a further reduction in contrail formation.

Using the chemical equilibrium for complete combustion of Jet A with a generic hydrocarbon composition[34], the amount of water from combustion can be determined.

$$C_{11.4}H_{21.7} + 16.825\,O_2 \longrightarrow 10.85\,H_2O + 11.4\,CO_2 \tag{4.48}$$

The mass ratio of water produced by combustion per unit of fuel is determined using the molar ratio from Eq. 4.48 and the molar mass of both species as per Table C.1:

$$\frac{\dot{m}^w_{comb}}{\dot{m}_{fuel}} = \frac{10.85\ M_{H_2O}}{11.4 * M_C + 21.7 * M_H} = \frac{10.85 * 18.0153}{11.4 * 12.011 + 21.7 * 1.00794} = 1.2309 \tag{4.49}$$

$$\dot{m}^w_{comb} = 1.2309\ \dot{m}_{fuel} = 1.2309\ SFC \cdot F_n \tag{4.50}$$

Where $\dot{m}^w_{comb}$ is the mass flow of water generated by combustion, $\dot{m}_{fuel}$ is the fuel flow into the combustor; M_{H_2O}, M_C, M_H are the molar masses of water, carbon, and hydrogen, respectively.

Schumann showed that an increase in propulsive efficiency leads to an increase in threshold temperature for contrail formation [35], meaning that contrails can be formed at higher ambient temperature. Even though higher efficiency engines have a lower consumption and therefore lower water content in the exhaust gases, they also have lower temperature exhaust gases. This leads to a net increase in frequency of contrail formation. Therefore, the most reliable way to reduce the likelihood of contrail formation is to reduce the water content in the exhaust gases.

4.7. Steam turbine

In order to extract the most work from the steam turbine, its pressure ratio must be maximized. The design pressure ratio is selected so that the injected steam has an overpressure of 1 bar over the dry air at the injection point.

4.8. Complete model

The model is assembled as shown in Figure 2.2.In the water loop between the condenser and the water pump, one more component is included. It acts as a way to close the water loop in NPSS while also adding necessary water or evacuating if there is excess. The added water is at the same pressure and temperature as the water that exits the condenser.

4.8.1. System Constraints

A constraint on the model was necessary to ensure that the solver did not go into a design space with nonphysical solutions or solutions that are incorrect with the chosen assumptions.

In the application of the SIWRT, it is important that water is liquid (x<0) through the pump before the evaporator. And to maximize the amount of work that can be extracted, the water would have to reach superheated steam (x>1) state after the evaporator. Expansion in the turbine leads to a reduction in vapor quality, but to avoid erosion of the steam turbine blades[36] and to maximize the work, the steam still needs to be vapor throughout the expansion in the turbine.

In order to ensure that the injected water is a superheated vapor, the pressure rise of the water pump was constrained to ensure the following condition:

$$x_{w25} \leq 1.02 \tag{4.51}$$

Where x_{w25} is the vapor quality of the water at station w25, right before injection into the air stream.

4.8.2. Operating Condition: Top of Climb

Typically the flow sizing point of turbofans is Top of Climb (ToC). This point is at cruise altitude but high thrust. Typically the engine is at its highest OPR under normal operation. Sizing the engine at ToC, allows for fixing the design and then running any other operating condition in an off-design setting. Figure 4.4 shows a typical mission profile with top of climb highlighted.

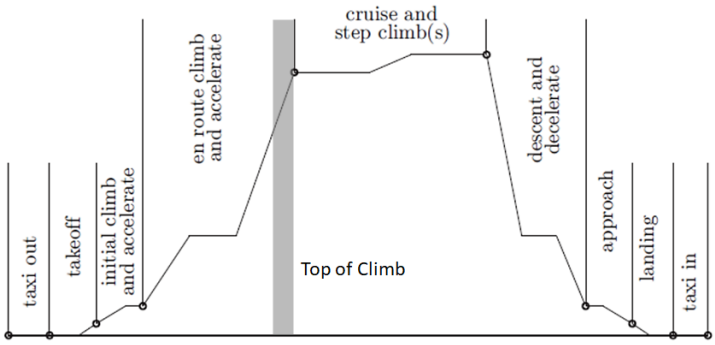

Figure 4.4: A typical commercial flight mission profile[37] with highlighted top of climb.

5

Verification and Validation

Verification is the process of determining if a simulated process is performing the calculations as intended. Validation typically follows after and it consists of determining if a simulated process represents the real life process. Verification and validation (V&V) are key to translating a simulated system to a real life working example. Ideally, every single component of a system would go through V&V, however that is often very cumbersome and not always time and resource efficient. In the current study, many of the system components that are used are provided by NPSS, it can be assumed that they are verified and validated before the software was released. The components that are chosen to go though V&V in this study are the evaporator and condenser. This is because they are the most complex to model and are key to the working principle and performance of the SIWRT concept.

5.1. Verification

This section goes over the verification steps for the evaporator and condenser to ensure that the written code in the component is performing the intended calculations.

5.1.1. NTU method - Evaporator

The evaporator and condenser's variable heat capacity NTU approach is mirrored using Microsoft Excel with a miniREFPROP add-in for species properties. The results are compared with the results given by the NPSS components. Additionally, the iteration steps in the heat exchangers' nested solvers are not modeled in the verification process. However the design space of the solver is established and the solver terms can be shown. The verification was done with dry air instead of humid exhaust gases, as the properties of humid air are easier to mirror external to NPSS. The results of the evaporator verification are given in Table 5.1.

The nested solver in the evaporator uses an outlet enthalpy guess. Knowing the outlet conditions, the effectiveness ε is determined. Additionally, the mean properties of each stream are determined for the ε-NTU method, which outputs another value for effectiveness: ε_{NTU}. The solver finds the outlet conditions where the two values of effectiveness are equal, by minimizing the absolute difference between them. Inlet conditions expected in the evaporator are chosen and verifying calculations are performed.

Figure 5.1 shows the variation in effectiveness for the different outlet conditions: The linear increase in ε is as expected due to its linear dependence on the heat transferred. Initial dip in the ε_{NTU} curve is caused by the boiling process: theoretically heat capacity during phase change is infinite, which is why the approach used takes the mean heat capacity between inlet and outlet, providing a finite, though steeply increasing value for $\overline{Cp}$. The minimum of the ε_{NTU} curve is found when the outlet conditions are no longer dual-phase, but rather superheated vapor. The heat capacity at that point is lower than that of liquid, rapidly reducing $\overline{Cp}$ until the curve converges to a value of 1. Observing this case brought to attention the possibility that the two curves may, under certain conditions, intersect more than once, providing more than one solution. Therefore the inlet conditions were varied to investigate this effect and the solution space further.

Table 5.1: Evaporator verification results for given inlet conditions. Outlet conditions determined by NPSS component and separate verification approach given in parentheses.

			Stream 1	Stream 2
	Properties		Dry air	Water
Inlet	T	[K]	800	304
	P	[MPa]	0.03	2
	$\dot{m}$	[kg/s]	40	3
Outlet	T	[K]	630.64 (630.7)	480.26 (480.26)
	P	[MPa]	0.0285	1.8
	$\dot{m}$	[kg/s]	40	3
Heat exchanger	U	[W/m^2K]	100	
	A_h	[m^2]	1	
	dP/P	[-]	0.05	0.1
	Q	[W]	7306.74 (7304.3)	
	ε	[-]	0.717 (0.717)	

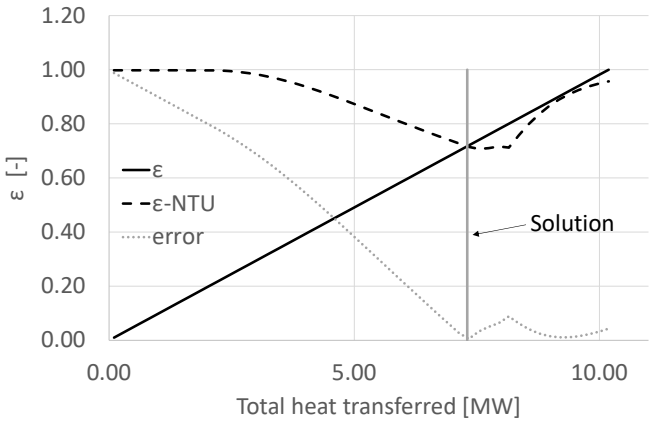

Figure 5.1: Evaporator nested solver finds the solution where the two methods of calculating effectiveness give the same result. This is where their curves intersect and the error is within tolerance.

Provided in Figure 5.2 are all possible solutions provided by this approach for a range of air inlet conditions. For $T_{air,in} \leq 800K$, there is only a single solution, with the water at the outlet is a dual-phase fluid. For $T_{air,in} \geq 1000K$ there is a single solution, where the water at the outlet is a superheated vapor. For the range $800K < T_{air,in} < 1000K$, there are 3 solutions, where the water outlet varies from dual-phase fluid to superheated steam. The solver in the evaporator component is capable of finding only one solution which is determined by its initial guess. Two methods are shown in Figure 5.2 that use different solver initial guess for ε_0:

- NPSS0: $\varepsilon_0 = 0$
- NPSS1: $\varepsilon_0 = 1$

In the range where multiple solutions exist, NPSS0 finds the lowest value, while NPSS1 finds the highest value.

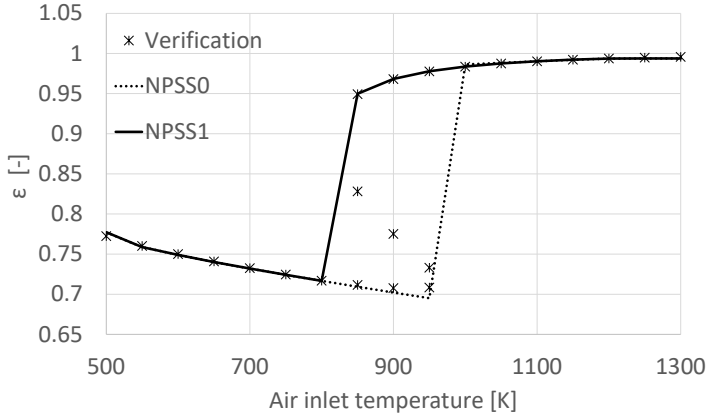

Figure 5.2: Comparison between the verified results and NPSS component results for a varying air inlet temperature. NPSS0 uses an iteration initial value for effectiveness zero, NPSS1 uses an iteration initial value for effectiveness of one, and stars shows all possible solutions per set of inlet conditions.

It is difficult to determine which single solution is correct or close to the physical answer because the used approach at its base is a simplification of the water temperature profile inside the heat exchanger. It can be argued that the simplification for water temperature profile leads to higher discrepancies when the water is still boiling at the outlet as opposed to a superheated steam. And the higher the steam temperature, the more accurate the approach is. Additionally, solutions with dual-phase fluid or insufficient superheating of the steam are filtered on a system model level. This is because the water stream exiting the evaporator goes into a steam turbine, after which it still needs to be a superheated vapor for injection. It appears that multiple solutions occur only when the water outlet conditions are close to the saturated vapor line, which do not fulfill the system requirements in the first place. As a result, the evaporator nested solver is set up with initial guess at $\varepsilon = 1$, ensuring that the highest effectiveness value is found as a solution.

5.1.2. NTU - Condenser

The verification process of the condenser follows the same steps as the evaporator. The main difference is that the iteration guess is made on the humid air outlet temperature, as this provides a direct solution on the condensation and heat transferred. The verification runs use dry air as a cooling flow and humid air as the flow to be condensed. The results of the condenser verification are given in Table 5.2. The verified outlet temperature, pressure, mass flows, heat transfer rate, and effectiveness values are within 1% of the NPSS component. This can be attributed to rounding errors and differences in interpolation between the softwares. It is, however, enough to determine that the condenser component is verified and performs as intended.

Table 5.2: Condenser verification results for given inlet conditions. Outlet conditions determined by NPSS component and separate verification approach given in parentheses.

			Stream 1	Stream 2	
	Properties		Dry air	Humid air	Condensed water
Inlet	T	[K]	350	500	-
	P	[MPa]	0.5	0.5	-
	$\dot{m}$	[kg/s]	500	3	0
	WAR	[-]	0	0.3	-
Outlet	T	[K]	379.26	375.2 (375.26)	375.2 (375.26)
	P	[MPa]	0.45	0.45	0.45
	$\dot{m}$	[kg/s]	500	41.507 (41.523)	3.493 (3.477)
	WAR	[-]	0	0.199 (0.2)	-
Heat exchanger	U	[W/m^2K]	100		
	dP/P	[-]	0.05	0.1	-
	A_h	[m^2]	1		
	Q	[W]	14769.05 (14783.53)		
	ε	[-]	0.543 (0.543)		

Figure 5.3 shows the results from an iteration loop for a single case and Figure 5.4 shows the amount of condensed water for the same iteration loop. It can be seen that for low heat transfer rate it there is no water condensed, because the outlet temperature is not low enough. When conditions allow for water to be condensed, the heat required to achieve the same temperature change is increased. This is because the higher heat capacity of liquid water and the latent enthalpy of vaporization act as a heat sink. This effect can be seen in Figure 5.3, where the effectiveness is linearly increasing with the reduction in humid outlet down to 385K, after which further reduction in temperature requires more heat seen in the increased slope of the ε curve.

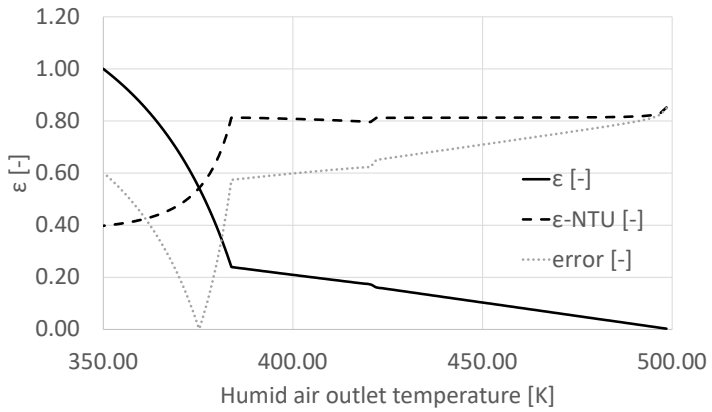

Figure 5.3: Condenser nested solver finds the solution where the two effectiveness calculations are the same. This is where their curves intersect and the error is within tolerance.

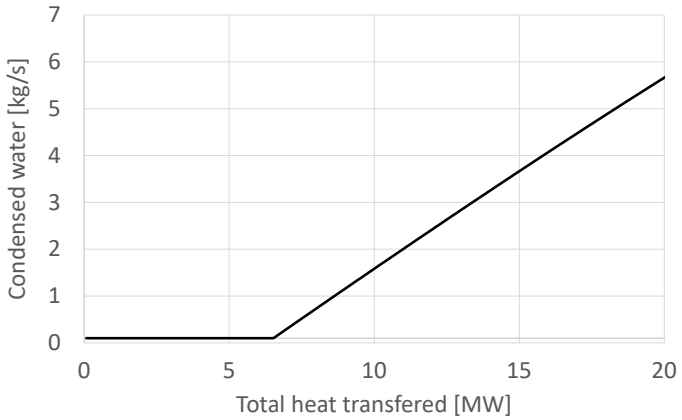

Figure 5.4: Rate of water condensation versus total heat transfer rate.

5.2. Validation

The best validation approach is to use an experimental setup to compare the results of the simulation. When that is not available, a high level simulation (i.e. CFD) can be used. Unfortunately, no experiment or published CFD data was found on the evaporator and condenser. A study that uses a discretized NTU-ε for an evaporator for the WET engine was used to validate the evaporator component. While the condenser component could not be validated to the same degree, air humidity data was used to validate the water content in the outlet of the humid air.

5.2.1. Evaporator

Schmelcher M. et al [38] studied a heat recovery steam generator (HRSG) for the WET engine. The HSRG is an evaporator that is split into 600 cells each of which uses NTU-ε to determine heat transfer rate. It is referred to as the cell-based P-NTU method and is shown in Figure 5.5.

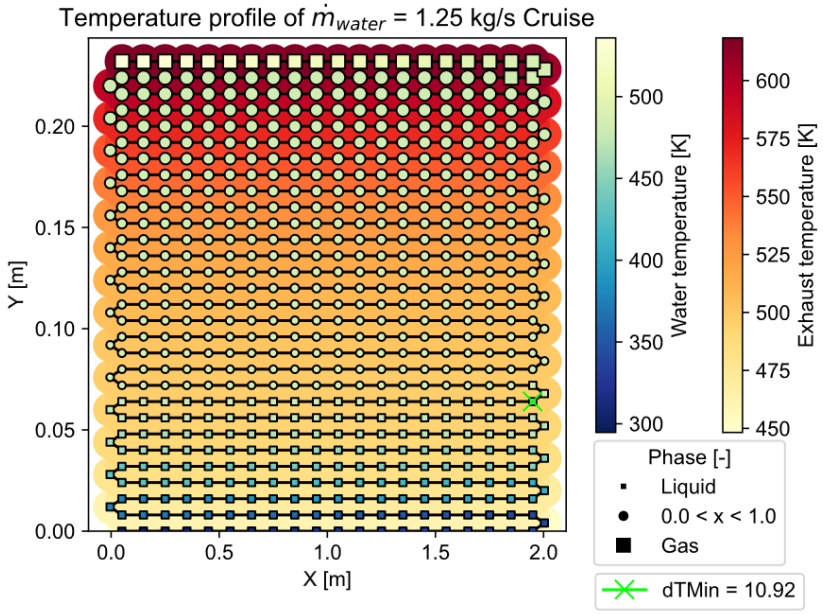

Figure 5.5: Schematic of the cell based P-NTU [38] approach used to validate the SIWRT evaporator.

There are two operating conditions where this heat exchanger is studied: Cruise and Maximum Take-Off (MTO). The inlet data is given in Table 5.3. Both operating points are applied in the evaporator which was created in NPSS.

Table 5.3: Inlet conditions of both streams for Cruise and MTO [38].

			Cruise	MTO
Exhaust gas	$\dot{m}$	[kg/s]	18.9	49.7
	WAR	[-]	0	0
	T	[K]	625	802
	P	[Pa]	35700	125700
Water	$\dot{m}$	[kg/s]	0-5	0-1.4
	T	[K]	293.15	293.15
	P	[Pa]	2000000	2000000

Using $U \cdot A_h = 90kW/K$ for the evaporator, the resulting exhaust gas outlet temperatures compared to the validation source are given in Table 5.4:

Table 5.4: Evaporator validation data [38] compared to SIWRT evaporator component output.

$\dot{m}_w$	[kg/s]	0.5	1.25	3	Data source
$T_{exh,out}$	[K]	625	537	480.3	P-NTU
		625	585	480.3	SIWRT

It shows good agreement for the $\dot{m}_w$ values of 0.5 and 3 kg/s. But for $\dot{m}_w = 1.25kg/s$ the SIWRT evaporator outputs 9% higher value for the exhaust gas outlet temperature. In order to have a better understanding of these results: Figure 5.6 shows a plot with the resulting outlet conditions and heat transfer rate for a range of water mass flow rate. There are three distinct regions of interest in the evaporator:

1. $\dot{m}_w \leq 1.1$ kg/s: the low water mass flow means that all of it can be heated up to the exhaust gas inlet temperature. This means an effectiveness $\varepsilon = 1$ or very close to 1. Water is a superheated vapor and the heat exchanger is oversized for the given conditions.
2. 1.1 kg/s < $\dot{m}_w$ < 1.35 kg/s: Water is a superheated vapor but has not reached the maximum possible temperature.
3. $\dot{m}_w \geq 1.35$ kg/s: Water is dual phase. Temperature is determined by water properties at the given pressure.

The SIWRT evaporator accurately determines the temperature of the water in regions 1 and 3. Since effectiveness is very close to 1, the heat transfer rate is determined by the properties of the water. The temperature in region 3 is determined accurately but the heat transfer rate is not, which is seen in the different water outlet steam quality. This is again a case where the water properties determine the temperature. Poor agreement in region 3 was expected, and as already mentioned in subsection 5.1.1 that is not a region of interest for the system model. However region of high interest for the system model is region 2. The results show agreement in trend and slope. Initially the water outlet temperature is lower than data, after which it grows to values higher than data, before promptly dropping. The final drop is likely due to the inherent discontinuity in the method employed, shown in Figure 5.2.

For maximum take-off, the study used for validation investigates water mass flow up to 1.4 kg/s, results of which are shown in Figure 5.7. The results of the SIWRT evaporator agree completely with the results. Although it is important to note that this range of mass flow corresponds to region 1 in the cruise operating point, which is an oversized heat exchanger and an effectiveness $\varepsilon = 1$. There is insufficient data to validate regions 2 and 3.

5.2.2. Humidity

As described in Section 4.3, the condenser in the SIWRT is a more complex device than most condensers found in literature. This is due to the fact that the SIWRT condenses and separates only one specie from a gas mixture. No literature was found on the performance of such a heat exchanger to use as source of validation. This is why only the humidity calculation part of the condenser component is validated. Using humid air, the percentage humidity was determined:

$$WGR_{\%} = 100\frac{WGR}{WGR^{sat}} \tag{5.1}$$

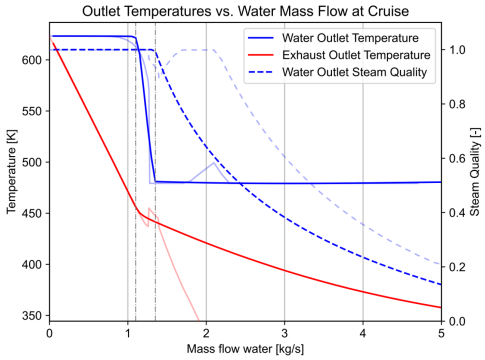

(a) Evaporator outlet conditions for varying water mass flow levels.

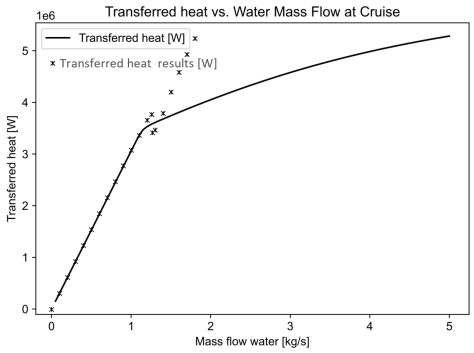

(b) Total heat transferred for varying water mass flow.

Figure 5.6: Validation results for cruise: validation data [38] given by opaque lines, results from the variable Cp NTU method given by transparent lines.

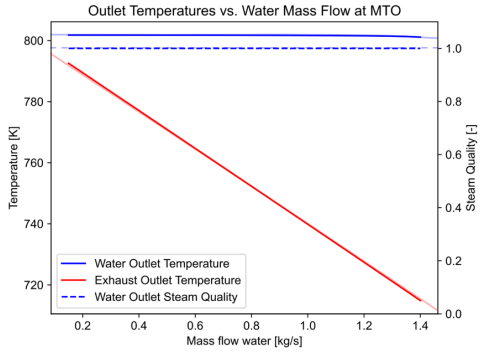

(a) Evaporator outlet conditions for varying water mass flow levels.

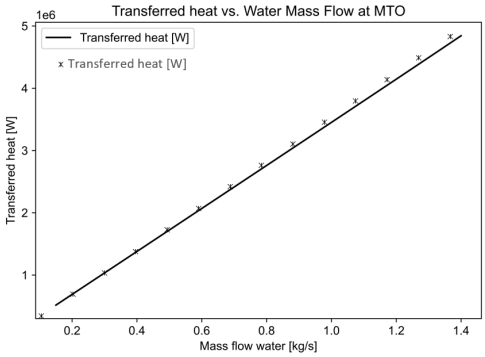

(b) Total heat transferred for varying water mass flow.

Figure 5.7: Validation results for take-off: validation data [38] given by opaque lines, results from the variable Cp NTU method given by transparent lines.

Where $WGR_{\%}$ is percentage humidity. For the temperature range of 30°- 100° C at sealevel pressure, the absolute humidity was determined for varying percentage humidity values. The results were compared to a psychrometric chart for humid air [28], shown in Figure 5.8:

The results show overall good agreement with data. Above 80° C at 10% percentage humidity, the absolute humidity is overestimated by a maximum of around 20%. At even higher temperatures, however, the values converge once again. Similar effect, but to a lesser degree of overestimation, can be observed for percentage humidity of 5% and 2% for temperatures above 90° C and 95° C, respectively.

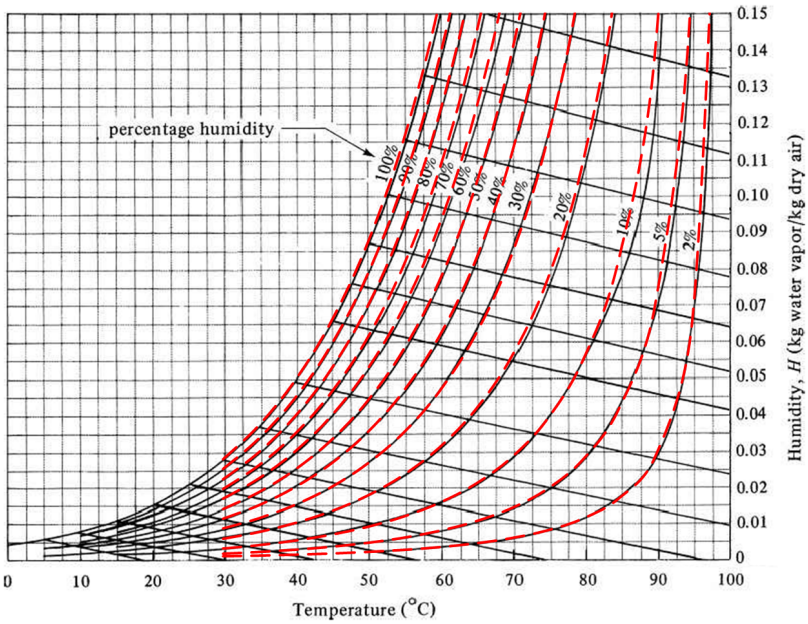

Figure 5.8: Psychrometric chart for air humidity, measured at sealevel [28]. Humidity results from the condenser are overlayed by dotted lines.

6

Results

After performing many simulations for varying WAR values, in this chapter the results are presented. The design point was chosen as a hot day top of climb (TOC):

- h = 10668m
- T_{amb} = ISA + 10K
- M_N = 0.84

The RM400 engine, researched and modeled at GKN Aerospace, is chosen as a reference engine. It is an ultra high bypass ratio (UHBPR) geared turbofan that follows the current engine design trends of increasing bypass ratio. The SIWRT matches the RM400 in most component performance parameters, however a few have been changed with the implementation of the water loop. An overview is shown in Table 6.1. Overall pressure ratio (OPR) was reduced by lowering the pressure ratio of the high pressure compressor. This is done so that the cycle can retain more heat in the flow after the LPT to be used for the recovery. Although, reduction in pressure also has a beneficial effect on NOx emissions [14]. Kaiser et al. [11], in their WET engine study, imply a reduction in OPR from a conventional engine after implementation of the water loop and show a reduction in NOx due to the pressure component. The OPR reduction in the SIWRT with from the RM400 was chosen to match the same reduction in the pressure component of NOx.

T_4 is also reduced in the baseline as the increased mass flow due to steam injection increases the specific power of the turbine, reducing the need for very high temperatures. However, higher values are still explored later on. FPR is reduced to enhance the possibility for water condensation by reducing the temperature of the cooling flow in the condenser. Additionally, this is a design trend that follows from conventional engines, where FPR is reduced with increasing FBPR. A new parameter is introduced with the SIWRT: condenser bypass ratio (CBPR). Since the bypass flow is further split before the condenser, this split is defined by a bypass ratio. It was not obvious from the start what a reasonable value would be. During the making of the model there was the intention to study the effects of varying it. Ideally, the condenser should be as small as possible, therefore the lowest possible cooling flow would have to be used. CBPR = 5 was found to be the highest value[1] for which water can be condensed, however, at this stage and in this report that could not be realized.

The SIWRT is required to generate the same net thrust as the RM400. In reality, the SIWRT is likely to have a higher thrust requirement as it is expected to weigh more, adding to the total weight of the aircraft directly and indirectly. Without a thorough engine weight and aircraft trade factor study it is impossible to determine what the SIWRT's thrust requirement would be, therefore, in this preliminary study the thrust is kept the same as the reference.

6.1. Amount of injected steam

In this study, the amount of injected steam is defined as the mass water to air ratio at station 31 (combustor air inlet), which shall be referred to simply as 'WAR' from now on. The WAR and FBPR were varied as independent parameters and solved for the mass flow at fixed thrust. Due to difficulties with solver stability, the model was unstable at high amounts of steam injection. The maximum WAR reached was 7%. The trends in the results, as well as previously published studies, indicate that a lower

[1] Because it is defined as a bypass ratio, the value for CBPR is the ratio of the air that bypasses the condenser over the air that goes in. Therefore, larger values for CBPR represent a smaller condenser with less air mass flow through it.

Table 6.1: RM-400 and baseline SIWRT engine specifications

	SIWRT	RM400	units
OPR	48	74	-
T_4	1700	1903.77	K
FBPR	-	13.7	-
CBPR	5	-	-
$PR_{BP\ fan}$	1.4	1.44	-
$PR_{core\ fan}$	1.3		-
PR_{LPC}	3.5		-
PR_{HPC}	10.76	16.59	-
Fuel	Kerosene		
LHV	43		MJ/kg
$\eta_{BP\ fan}$	0.9158		-
$\eta_{core\ fan}$	0.8754		-
η_{LPC}	0.8872		-
η_{HPC}	0.8695		-
η_{HPT}	0.93		-
η_{LPT}	0.935		-
η_{comb}	0.9995		-
F_{net}	67.35		kN

fuel consumption may be achieved by injecting more steam. Unfortunately, this improvement and the possible optimum design could not be quantified due to the lack of model convergence. However, increased water air ratio would require a larger evaporator which would increase weight and pressure drop. As this was not investigated, it is not clear if the increased WAR would be beneficial for overall engine performance or not.

Figure 6.1 shows the thrust-specific fuel consumption (SFC) across a range of WAR. At a fixed WAR, increasing FBPR leads to a reduction of SFC. This reduction eventually reaches a minimum, after which a higher FBPR leads to an increase in consumption. The values to the right of each minima is is not of interest, which is why when a minimum was found, the sweep was stopped and the solver moved to the next WAR value. This was also done to avoid instabilities with the solver.

Increasing the amount of injected water increases the efficiency and the specific power of the core, allowing a reduction of core size, which results in an increase of FBPR. As the water air ratio increases there is a weak trend of diminishing return, i.e. less improvement per increased percent of WAR, indicating that the design is moving in a direction of an optimum. Then the overall size of the engine increases in order to generate the required thrust, which leads to higher consumption. This engine was not sized geometrically; however, a parameter indicating the engine and fan size is the mass flow through the inlet (station 2). This is shown in Figure 6.2a.

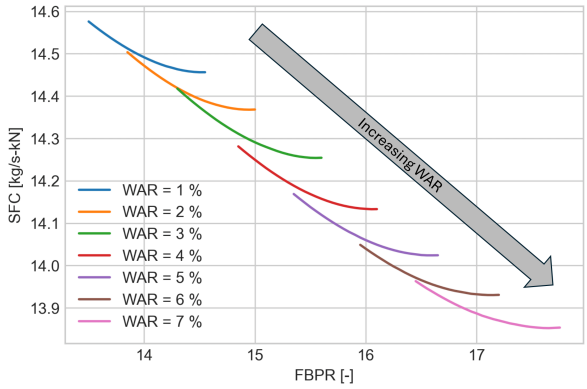

Figure 6.1: Specific fuel consumption vs. fan bypass ratio at different WAR values. Each curve is stopped after the minimum point, as an increase in SFC to the right is not of interest.

Higher WAR moves the curve minimum to a lower SFC and higher FBPR values. The added steam injection reduces the temperature of the now humid air that enters the combustion chamber. In addition, the heat capacity of the air increases as a result of the presence of water vapor. In order to keep the

turbine inlet temperature the same, the system requires an increase in fuel flow, leading to higher power generated for the same core size. However, in order to generate the required thrust, the design instead leads to a decrease in core size (seen in Figure 6.2b), while the fan size remains mostly the same.

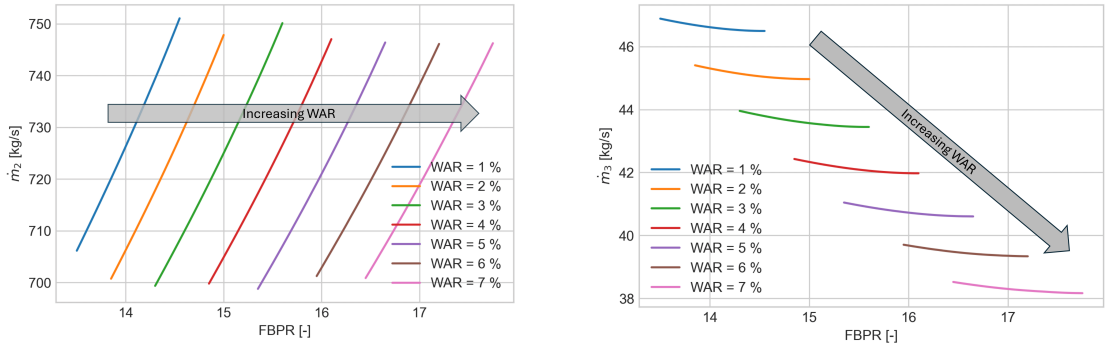

(a) Fan mass flow at different WAR.

(b) Core mass flow at different WAR.

Figure 6.2: Engine mass flows at different WAR.

Humid exhaust gases contain more water, meaning a higher density and heat capacity of the working fluid, increasing the potential for more work by the turbines. The increase in LPT specific power with an increase in WAR can be seen in Figure 6.3.

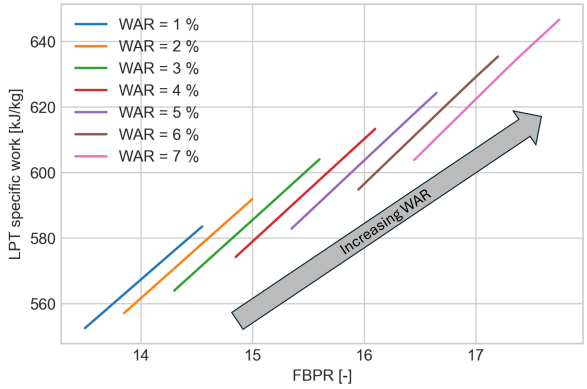

Figure 6.3: LPT specific work vs. fan bypass ratio at different WAR values.

Figure 6.4 shows the turbine power at different WAR values. At fixed WAR, the power generated reduces with FBPR. This is heavily influenced by the reducing temperature of the LPT, leaving less heat to be transferred in the water cycle. Increasing WAR does lead to an increase of steam turbine power, as there is a higher mass flow of the working fluid. The benefit appears to be lower and lower at higher WAR values. It is important to note that under these conditions, the system constraint on the vapor quality of the injected water is active. This means that the water pump pressure rise is reduced, reducing the ability of the cycle to generate more power.

The heat exchangers are modeled to have a constant overall heat transfer coefficient and the heat transfer area scales proportionally with the mass flow of the larger flow. Figure 6.5a shows the evaporator effectiveness versus FBPR for different WAR values. At a fixed WAR, increase in FBPR leads to a reduction in effectiveness. This is due to the fact that the higher work extracted by the LPT leaves the exhaust gases at a lower temperature, reducing the maximum possible heat that can be transferred. Increasing WAR leads to a trend with initially increasing effectiveness after it reaches a peak and reduces. The initial increase was found to be the result of non-physical solutions that result in the assumption of adding water into the system. As seen from Figure 6.7, there is no water condensed for the 1% and 2% and partially for the 3% WAR designs due to insufficient cooling. The system is designed to supplement the water needed to sustain the water loop from an infinite tank with the same pressure and temperature as the condensed water. The condition where no water is condensed the condenser outlet for the exhaust gas is at a significantly higher temperature, compared to cases where water is condensed. This results in all of the water in the loop to be supplied at a higher temperature, which is why the effectiveness is lower. Because these solutions are not useful for understanding the cycle they can be ignored. They were kept in this study because they explain some results, although non-physical,

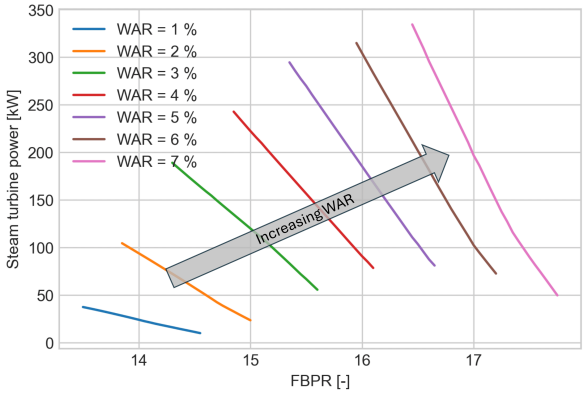

Figure 6.4: Steam turbine work at different WAR.

leading to a better understanding of this cycle and its sensitivity to the new water loop.

Figure 6.5b shows the total heat transfer for different WAR values. At fixed WAR, Q_{evap} shows a clear reduction which is more pronounce at higher WAR. This is in line with the effectiveness and can be explain with the same reasons of reducing temperature of the exhaust gas with FBPR. An increase in WAR leads to a step increase in heat transfer rate. The step increase is initially proportional to the mass flow of water, but the step size is reduced at higher WAR.

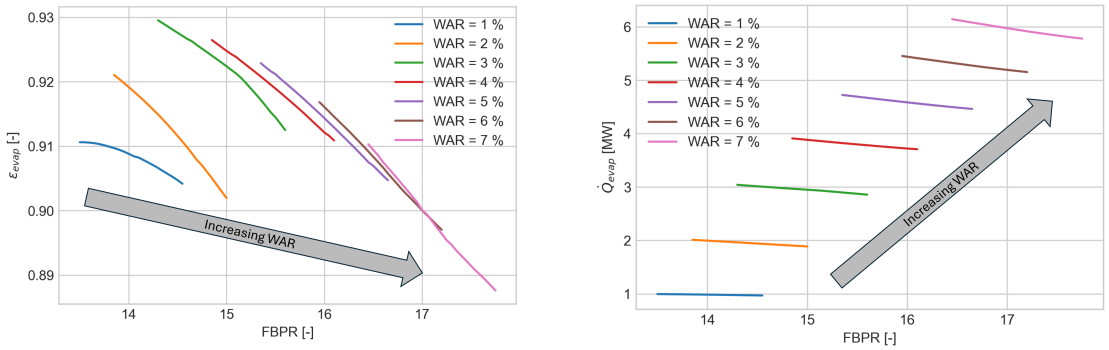

(a) Evaporator effectiveness vs. bypass ratio at different WAR values. **(b)** Evaporator heat transfer rate vs. bypass ratio at different WAR values.

Figure 6.5: Evaporator performance at different WAR.

The condenser effectiveness, on the other hand, shows an increase with FBPR, seen in Figure 6.6a. This is to be expected, as the condenser takes a part of the bypass flow at a constant condenser bypass ratio (CBPR), therefore a relative increase in bypass flow mass flow leads to a proportional mass flow increase in cooling flow to the heat exchanger. In addition, the limiting flow is the humid exhaust gas, which becomes relatively smaller at high fan bypass ratios. The combined effect leads to an increase in effectiveness. Subsequently, the relatively lower mass flow of exhaust gases means that there is less heat to be transferred, thus an increase in FBPR leads to a reduction in overall heat transfer rate, observed in Figure 6.6b.

Similarly to the evaporator, the effectiveness of the condenser initially increases with increasing water content in the exhaust gas, after which it starts to decrease. There is no such kink visible in the total heat transfer rate because the switch of increasing-decreasing effectiveness is due to how it is defined. At low WAR (and thus FBPR), there is no water condensed, but increasing WAR there is a point at which condensation is present. The condensation provides a potential for more heat to be transferred through latent heat of vaporization. This leads to the definition of effectiveness, which considers the ratios of the stream capacities of both streams, meaning that the more water is condensed, the higher the stream capacity is. The overall heat transfer rate of the condenser decreases with increasing WAR. This can be explained by the fact that higher WAR occurs at higher fan bypass ratios. At high FBPR, the core is smaller and not as much heat can be transferred.

Looking at the condensation rate of water, shown in Figure 6.7, it can be seen that at low humidity levels, no amount of water is condensed. The humidity of the exhaust gases is lower than the saturation humidity of the mixture. More water could be condensed if more heat is transferred out of the mixture. Higher WAR leads to higher humidity of the exhaust gases, meaning a larger overhead above saturation

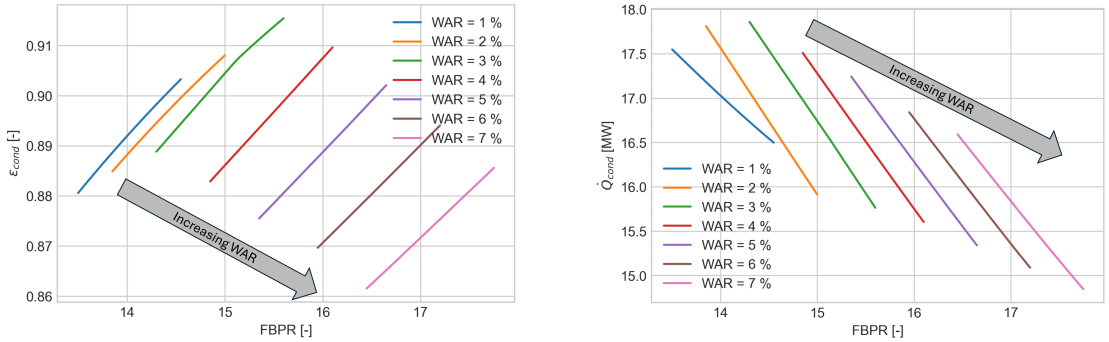

(a) Condenser effectiveness vs. bypass ratio at different WAR values. **(b)** Condenser heat transfer rate vs. bypass ratio at different WAR values.

Figure 6.6: Condenser performance at different WAR.

humidity, allowing for more of the water vapor to condense. As more water is condensed, latent heat is taken away from the water, resulting in a smaller temperature drop over the same heat transfer rate.

For a fixed humidity value where water condensation can occur, a higher FBPR leads to a smaller liquid water mass flow. The higher FBPR increases the power demand of the bypass fan relative to core size, leading to more work being exerted by the flow onto the LPT. This results in an exhaust gas with lower pressure and temperature at the LPT outlet. The lower temperature reduces the amount of heat available to heat up the water in the evaporator, seen in the reduction in the evaporator effectiveness and heat transfer rate with FBPR in Figure 6.5. The lower pressure in the humid exhaust gases requires a lower temperature in order to condense water, due to lower saturation temperature. This is due to the properties of water, where in order to have liquid water at lower pressures, the temperature needs to be lowered, as was observed in the saturated liquid line of water in Figure 3.4.

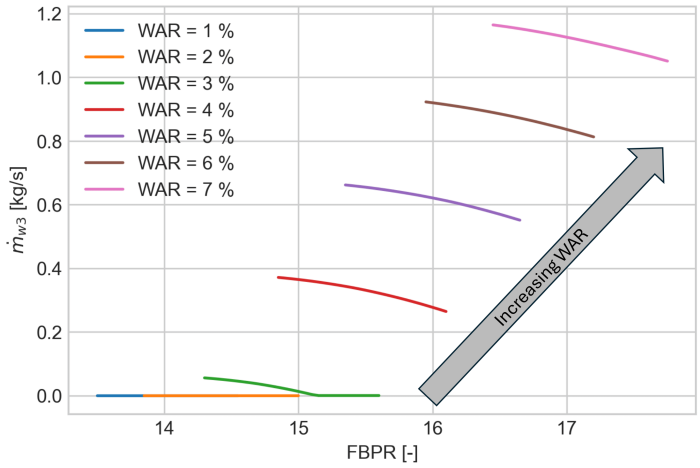

Figure 6.7: Amount of condensed water at different WAR.

6.2. Minimum SFC

In order to study the engine performance by varying engine design parameters, a single design point needs to be chosen for each WAR value. Figure 6.8 shows a generic SFC-FBPR curve with key design points for a conventional turbofan. Typically the design that results in minimum SFC is not chosen, but instead it is preferred to have a design with a lower bypass ratio, as that tends to yield a design with the lowest fuel burn over a mission. A further decrease in FBPR leads to a minimized maximum take-off weight (MTOW), and even more of a decrease leads to minimizing direct operating costs (DOC)[39]. In conventional engines empirical data can give an indication on how much the FBPR must be to be close to a given point. Unfortunately, because the data is based on existing engines and the SIWRT is far from conventional. There are no operational aero engines with this cycle at the moment, therefore, it is unknown if these points of interest are located in similar locations. Determining this would require a weight and sizing study on the engine and its integration onto an aircraft, which is beyond the scope of this thesis. This is why, in order to study the performance characteristics of the SIWRT, the minimum

SFC point is chosen from this point onward. This results in the minimum SFC line in Figure 6.9.

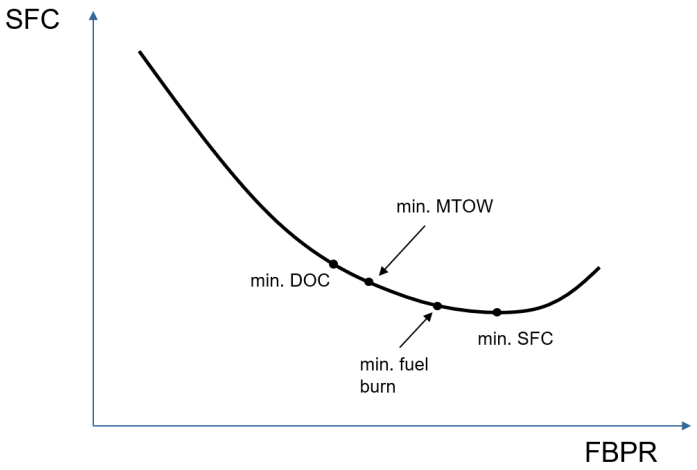

Figure 6.8: Example SFC vs. FBPR curve with general location of design points of interest [39].

The same reduction in SFC with increase in WAR can be seen as before. At low WAR the SFC is higher than that of the RM400: 14.15 kg/s-kN. The added components introduce losses in the form of pressure drop. All pressure drop values in the RM400 and SIWRT are given in Appendix B and A, respectively. The point at which the benefit of including the water loop evens out the drawbacks of the introduced losses is at WAR ≈ 4%.

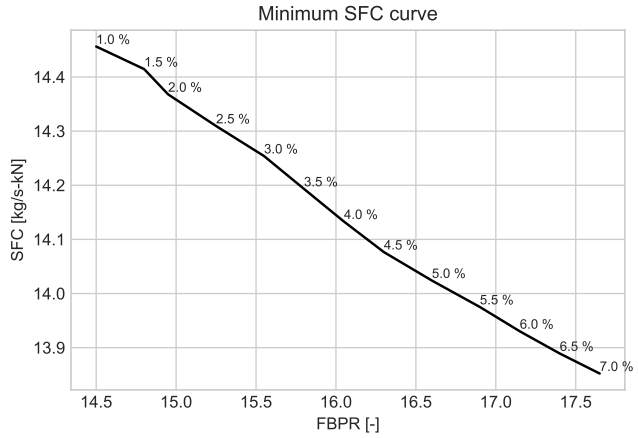

Figure 6.9: Baseline minimum SFC line vs FBPR for a range of WAR (given in percentages).

6.2.1. NOx emissions

There were several ways to estimate the NOx emissions, described in Section 4.6.1 that provide different results, shown in Figure 6.10.

- NPSS uses the P3T3 method without consideration for combustion air humidity. There is still a reduction with higher water content due to the temperature drop after steam injection and before combustor inlet.
- GasTurb 13 uses a simplified fuel flow method with the use of a steam correction factor based on WFR. This leads to a steep reduction in EINOx to almost zero at WAR = 7%.
- MTU uses a similar method to GasTurb with a technology factor TF = 0.72 and a steam correction factor based on experimental results. It shows a clear reduction in EINOx with added steam.

NPSS does not use combustion humidity, GasTurb method is more sensitive with respect to steam injection. Since the method used on the WET is the only one that is based on experimental results for humid combustion, it considered to be the most trustworthy method and is the one used to study the EINOx results of the SIWRT.

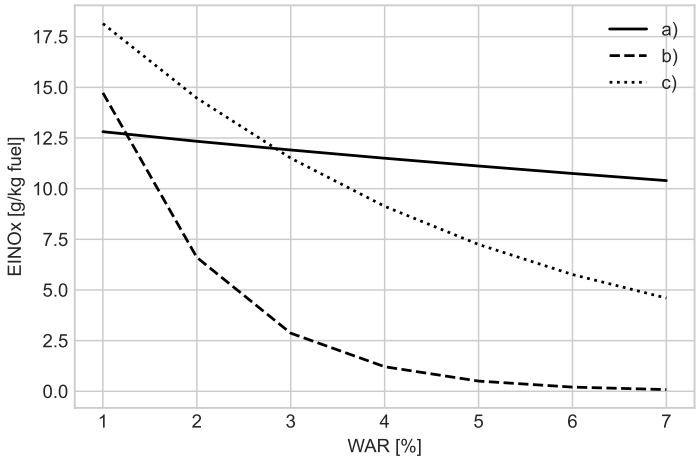

Figure 6.10: EINOx results vs WAR from different methods: a) is the method employed by NPSS, which does not take combustion humidity into account; b) is the P3T3 method with a steam correction factor based on water-fuel-ratio used by GasTurb 13; c) is the P3T3 method with a technology factor and a steam correction factor based on water-air-ratio, used by Kaiser S. et al [11].

6.3. Overall Pressure Ratio

In this section, the overall pressure ratio of the engine was varied by changing the pressure ratio of the HPC. Due to NPSS solver instability, only one value other than the baseline could be explored. This is sufficient to observe how OPR affects this cycle.

Figure 6.11 shows the SFC - FBPR carpet plot for varying WAR and two values of OPR. For a fixed WAR, an increase in the OPR leads to a reduction in SFC, mainly because of the increase in the thermodynamic efficiency of the Brayton cycle. Higher OPR designs also lead to higher pressure of the exhaust gases, which allows the core to generate more thrust. This results in a smaller fan and lower FBPR.

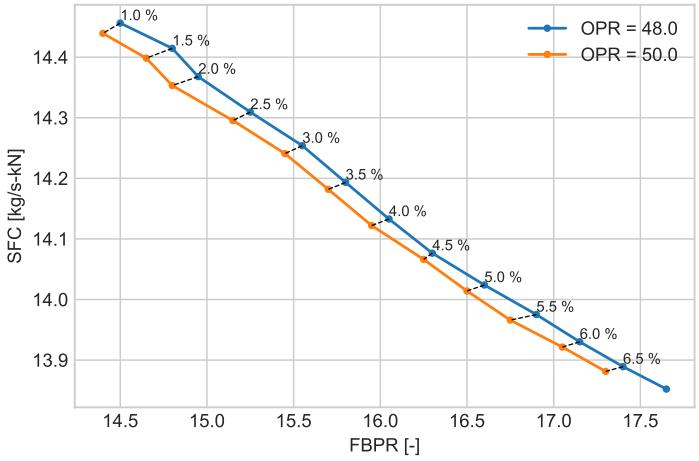

Figure 6.11: Minimum SFC line for varying overall pressure ratio and WAR values.

Figure 6.12a shows the evaporator effectiveness for different OPR values. It can be seen that increasing OPR leads to a reduction in evaporator effectiveness. This results from the fact that with higher OPR the HPT needs to extract more work from the flow, leading to a lower temperature at the outlet. Because the exhaust gases are used as a heat source and the water stream is the limiting fluid, effectiveness reduces. The reduction in OPR with respect to the reference engine was to retain more heat for the water recovery. Figure 6.12b shows the total heat transfer rate of the evaporator $\dot{Q}_{evap}$. The trend shows an increase in Q_{evap} with an increase in OPR for a fixed FBPR but does not show a significant difference for a fixed WAR. The increase at fixed FBPR comes from an increase in WAR, which is an increase in water mass flow. Because the reduction in effectiveness is small in comparison it leads to an absolute heat transfer increase.

Figure 6.13 shows the EINOx for a variation of OPR. At constant WAR, increasing OPR leads to an increase in EINOx, due to the pressure component, shown in eq. 4.44. However that increase is not

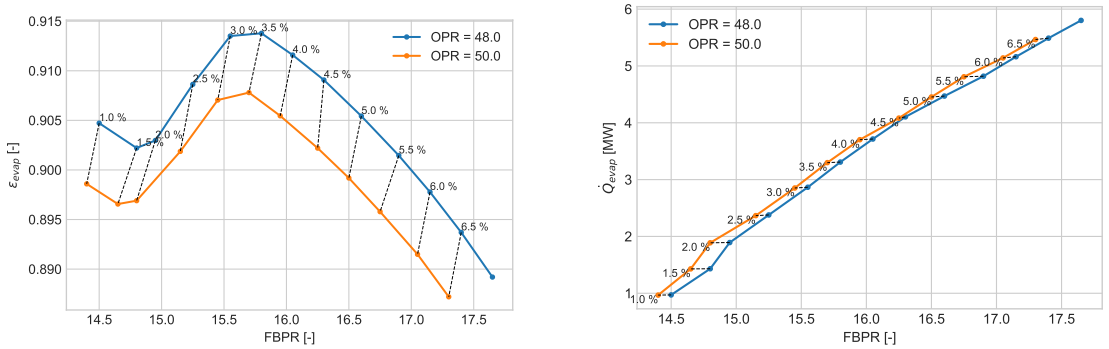

(a) Evaporator effectiveness vs fan bypass ratio for different overall pressure ratio and WAR values.

(b) Evaporator total heat transfer rate vs fan bypass ratio for different overall pressure and WAR values.

Figure 6.12: Evaporator performance at different OPR and WAR values.

very significant. Especially, considering it is a massive improvement from the RM400 EINOx value of 31.09 kg/kg fuel. The significant reduction in T_4 and OPR form the reference engine already leads to an EINOx of less than half, and any more added water leads to a further reduction.

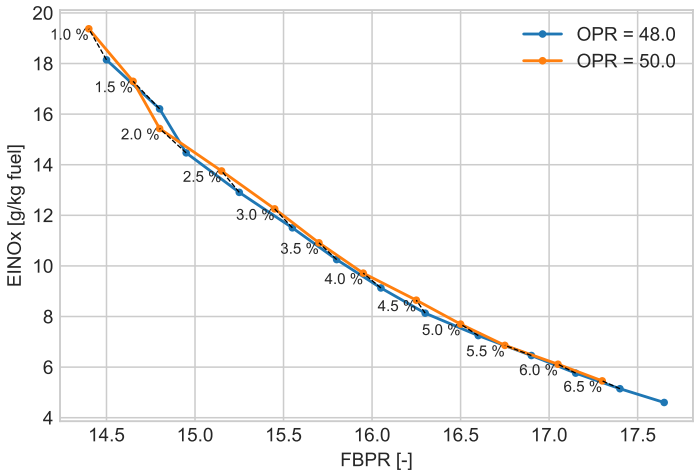

Figure 6.13: EINOx vs fan bypass ratio for different overall pressure ratio at different WAR values.

Figure 6.14 shows the power generated by the steam turbine for a variety of OPR. The increase in OPR leads to a reduction in the power extracted. The curve shows the same limitation as described in Section 6.1 with a further drawback due to the effects of higher OPR. This is once again caused by the lower temperature of the exhaust gases behind the LPT, which reduces the amount of heat transferred to the water flow, leading to a decrease in the amount of work that can be extracted from that flow. At both baseline and higher OPR, the injected steam quality constraint is also acting. This further reduces the expansion ratio of the steam turbine to ensure the injection of dry steam.

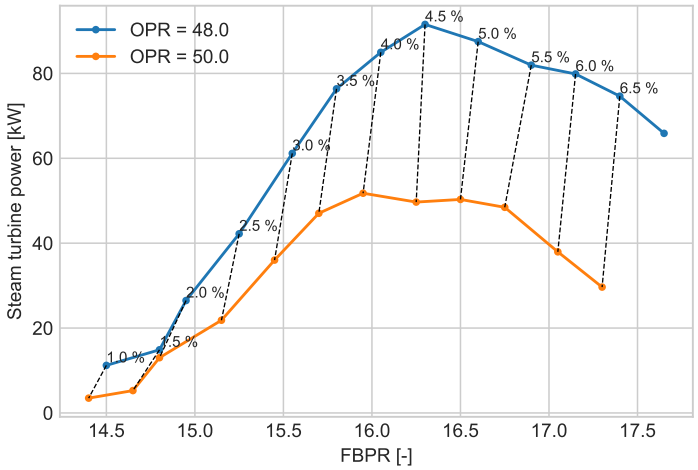

Figure 6.14: Steam turbine power vs fan bypass ratio for different overall pressure ratio at different WAR values.

Figure 6.15 shows the condenser performance, where 6.15a and 6.15b are the effectiveness and total heat transfer rate of the condenser versus fan bypass ratio, respectively. The effectiveness can be seen to be initially increase with FBPR up to a point where it sharply decreases. To the right of this peak is where water condensation occurs, resulting in a change in slope of the stream capacity ratio R in the heat exchanger. This switch is not intrinsically a physical change, but rather a definition change, confirmed by not appearing in the heat transfer rate. In the design space to the right of the peak, increase in OPR leads to a reduction in both effectiveness and heat transfer rate. This reduction is explained by the reduction in FBPR, which leaves less cooling flow in the condenser.

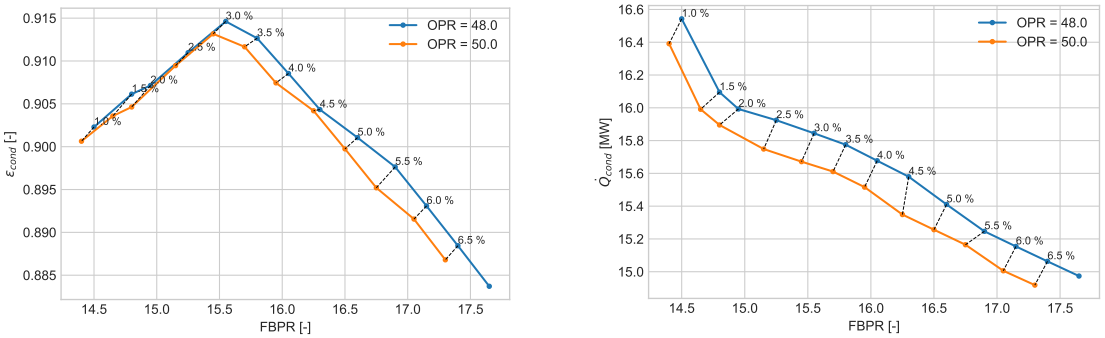

(a) Condenser effectiveness vs fan bypass ratio for different overall pressure ratio and WAR values.

(b) Condenser total heat transfer rate vs fan bypass ratio for different overall pressure ratio and WAR values.

Figure 6.15: Condenser performance at varying OPR and WAR values.

Figure 6.16a shows the liquid water mass flow output from the condenser, which can be considered as how much liquid water is created by the cycle. At low FBPR and WAR there is no water condensed, until a threshold, above which there is an increase in water condensation. At a fixed FBPR the increase in OPR leads to an increase in water production. This increase in $\dot{m}_{w3}$ is mainly due to the combined effect of higher water content and lower exhaust gas temperature. The higher WAR increases the saturation temperature of the mixture allowing water to condense at a higher temperature. At higher OPR that threshold for water condensation is at a lower FBPR, which means that higher OPR leads to slightly more water production. At a fixed WAR, the water condensation rate is lowered slightly. This is explained by the reduction in FBPR, which in turn reduces the cooling mass flow of the condenser, confirmed by the . Figure 6.16b shows the required water in order to sustain the cycle. It is a mass flow that is provided from a source external to the cycle. For low WAR where no water is produced the demand to supply water is increasing, however, once the condensation threshold is reached, the requirement becomes constant. At higher OPR the required water is higher, due to the lower water condensation rate.

Detailed data on the RM400 can be found in Appendix B and detailed data on the SIWRT can be found in Appendix A.

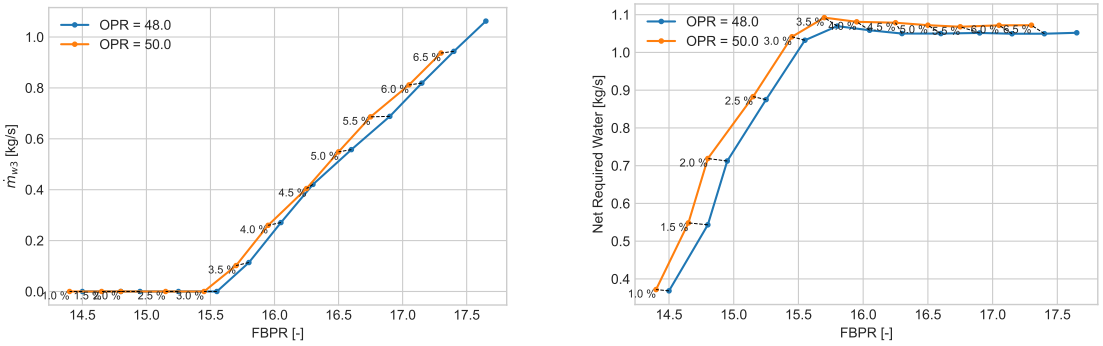

(a) Condenser liquid water mass flow output vs fan bypass ratio for different overall pressure ratio and WAR values.

(b) Required water to sustain water loop vs fan bypass ratio for different overall pressure ratio and WAR values.

Figure 6.16: Water cycle mass flow at different OPR and WAR values.

6.4. Combustor outlet temperature

One of the benefits of steam injection is the reduced combustor outlet temperature (T_4), which results from the water content in the air. This allows for the use of more fuel up to the temperatures of dry combustion, resulting more power being generated for the same size core. Because the SIWRT has the means to capture the extra heat from the exhaust gases, it benefits from higher T_4 more than a conventional engine. This section explores the effects of increasing the burner outlet temperature on the resulting designs.

Figure 6.17 shows the variation of SFC with FBPR at different combustor outlet temperatures. There is a clear reduction in SFC with increase in T_4 that comes as at a higher FBPR. Since the OPR of all these cases is equal, the higher T_4 leads to a bigger temperature rise in the combustor, increasing cycle efficiency. Additionally, the added heat means that more heat can be recovered through the cycle. The added cycle efficiency means that the core can be downsized and retaining a similarly sized fan. Together with the added heat into the bypass flow, the bypass nozzle generates additional thrust. The constant T_4 curves show a decrease in slope at higher WAR, indicating that a minimum exists at WAR > 7%. The $T_4 = 1700K$ curve's reduction in slope is at a lower FBPR and WAR, as it shows it is reducing in slope more rapidly than the remaining curves. At constant WAR, SFC is still reducing at higher T_4, however the rate of that reduction appears to be smaller between 1800 K and 1900 K.

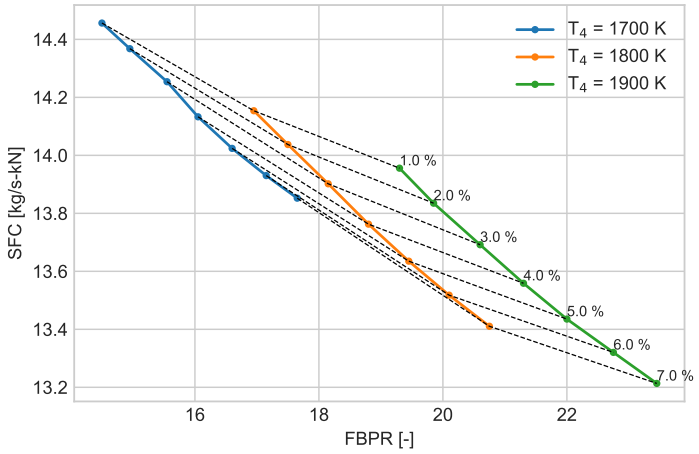

Figure 6.17: Specific fuel consumption versus fan bypass ratio at different combustor outlet temperature and WAR values.

The EINOx at different T_4 values can be seen in Figure 6.18. The increase in EINOx due to T_4 is relatively small compared to the reduction due to WAR. The small increase due to T_4 results from eq. 4.44 where the EINOx contributions are from the pressure and temperature at station 3, which remain mostly unchanged. There is a small variation in T_3 due to the varying temperature of the injected steam which has a small effect on the combustor inlet temperature.

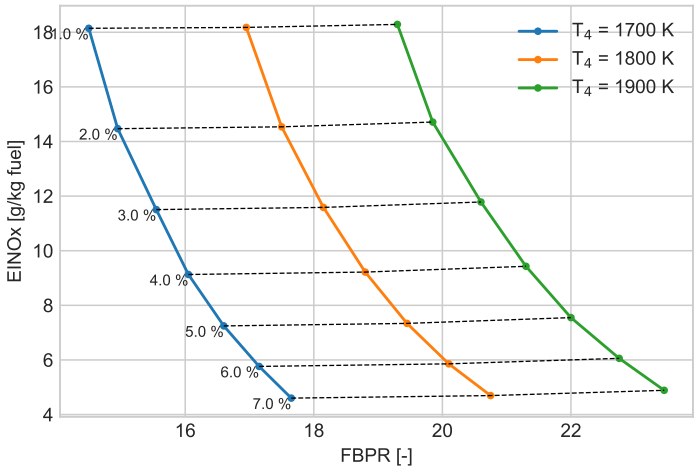

Figure 6.18: EINOx versus fan bypass ratio at different combustor outlet temperature and WAR values.

Figure 6.19 shows the evaporator performance for different combustor outlet temperature values, figure 6.19a shows the evaporator effectiveness, and figure 6.19b shows the overall heat transfer rate. Just as expected, the higher T_4 leads to a higher exhaust gas temperature to be used in the evaporator, increasing its effectiveness. The reduction in core size also means that there is less water mass flow, contributing to the high effectiveness.

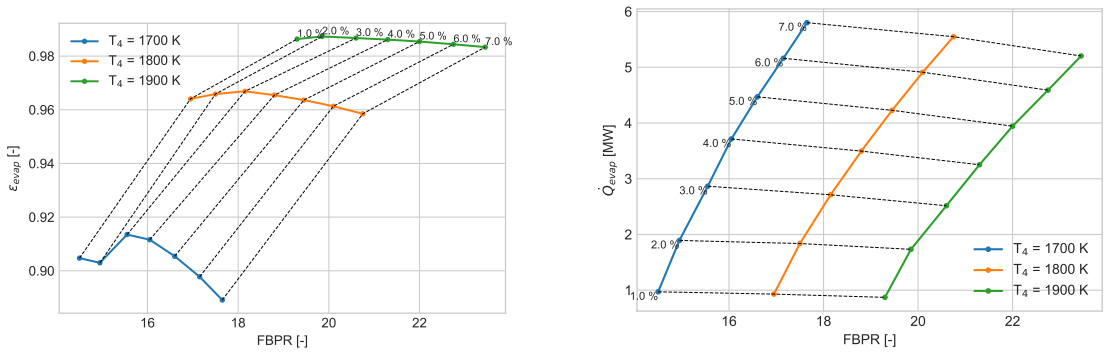

(a) Evaporator effectiveness vs fan bypass ratio for different combustor outlet temperature and WAR values.

(b) Evaporator total heat transfer rate vs fan bypass ratio for different combustor outlet temperature and WAR values.

Figure 6.19: Evaporator performance at varying combustor outlet temperature and WAR.

A full complete utilization of the water loop means that the work of the steam turbine is an interesting parameter to look at, shown in Figure 6.20. The lack of the means that for T_4 values above baseline 1700 K, significantly more power can be generated by the pump. The amount of power increases in a mostly linear dependence to WAR as that is related to the water mass flow. At a fixed WAR, from $T_4 = 1800K$ to $T_4 = 1900K$, the increase in power generated is small, because the steam turbine is sized to ensure overpressure of the injected steam. This indicates that an increase in water pressure may be beneficial in increasing the power generated by the steam turbine.

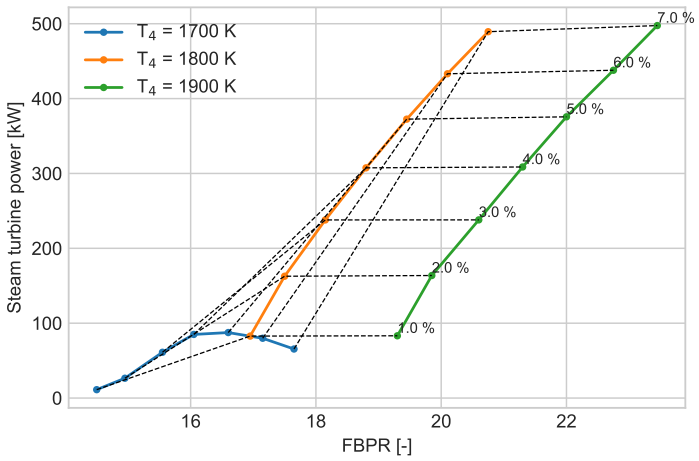

Figure 6.20: Steam turbine power versus fan bypass ratio at different combustor outlet temperature and WAR values.

Figure 6.21 shows the condenser performance at varying T_4 and WAR. Figure 6.21a shows the effectiveness, while figure 6.21b shows the total heat transfer rate $\dot{Q}_{cond}$. For a fixed WAR value, increase in combustor outlet temperature leads to an increase in evaporator effectiveness. That is in line with the increase in FBPR, which increases the amount of cooling flow in the condenser. The initial positive slope in each T_4 curve is the part where no water is condensed and to the right of the peak, water condensation occurs and increases with WAR. The limiting stream is the exhaust gas side, which changes stream capacity curve when condensed water is present. This is due to the latent heat of evaporation, creating a discontinuity between the temperature and enthalpy. The total heat transfer rate of the condenser appears to not vary as much with T_4. Although the larger FBPR provides more cooling flow, there is a lower exhaust gas mass flow, resulting in a small net difference in $\dot{Q}_{cond}$. This indicates that it may be possible to use a similarly sized heat exchanger at higher T_4, which would be beneficial for minimizing weight, but this is not clear without performing a relevant study.

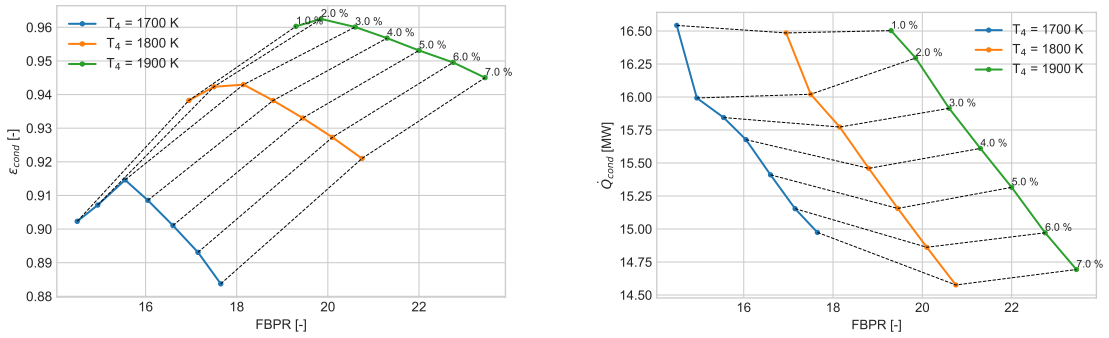

(a) Condenser effectiveness vs fan bypass ratio for different combustor outlet temperature and WAR values.

(b) Condenser total heat transfer rate vs fan bypass ratio for different combustor outlet temperature and WAR values.

Figure 6.21: Condenser performance at varying combustor outlet temperature and WAR.

Figure 6.22 shows the water loop mass flow for different T_4 values. Figure 6.22a is the liquid water created by the condenser and figure. An increase in combustor outlet temperature leads to a small increase in the amount of condensed water. As the condenser effectiveness is higher at higher T_4, the added cooling leads to an increase in the amount of condensed water. The added fuel flow leads to the production of additional in the combustor, contributing to the increase in the amount condensed from the exhaust gases. The increase in the amount of water condensed and the reduction in core size means that less water is required to supply the engine from an external tank, seen in Figure 6.22b.

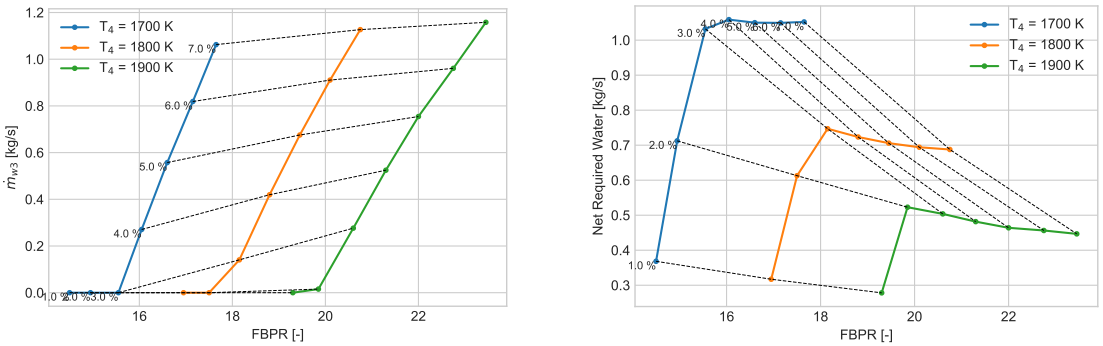

(a) Condenser liquid water mass flow output vs fan bypass ratio for different combustor outlet temperature and WAR values.

(b) Required water to sustain water loop vs fan bypass ratio for different combustor outlet temperature and WAR values.

Figure 6.22: Water cycle mass flow for varying combustor outlet temperature and WAR.

6.5. Fan Pressure Ratio

The high FBPR values and variability make it important to select an appropriate fan pressure ratio (FPR). Moreover, the bypass flow is used as a cooling flow in the condenser, which makes the choice of FPR critical to the performance of the SIWRT and its ability to self sustain its water loop.

The specific fuel consumption at different FPR and WAR can be seen in Figure 6.23. At a fixed WAR, the increase in FPR leads to an increase in SFC and a reduction in FBPR. This reduction in FBPR comes with a reduced BP mass flow, while keeping the core size mostly the same. Because the BP nozzle has a larger pressure ratio, it can generate the the required thrust with less mass flow. This is why conventional design trends reduce FPR with an increase in FBPR.

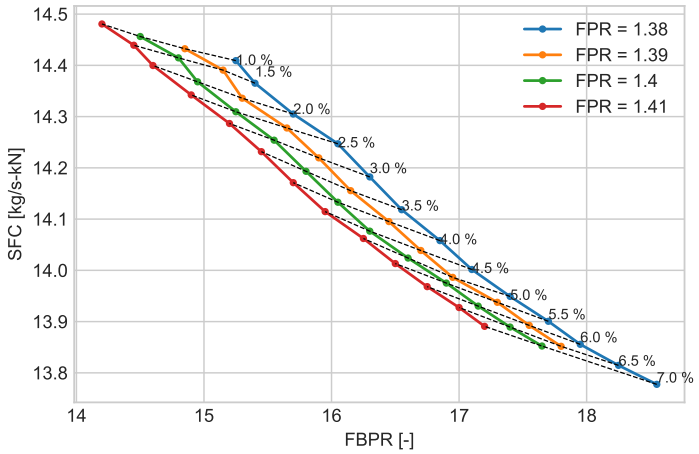

Figure 6.23: Specific fuel consumption versus fan bypass ratio at different fan pressure ratio and WAR values.

Figure 6.24 shows the EINOx versus FBPR at different FPR values. EINOx does not vary significantly with FPR at constant WAR. This is mainly because this change does not influence anything up to to and including the combustor, with the exception of the fuel flow. Therefore WAR is still the majority of the influence on NOx. It is important to note that EINOx is relative to fuel flow, therefore the increased SFC of higher FPR does mean higher absolute NOx production.

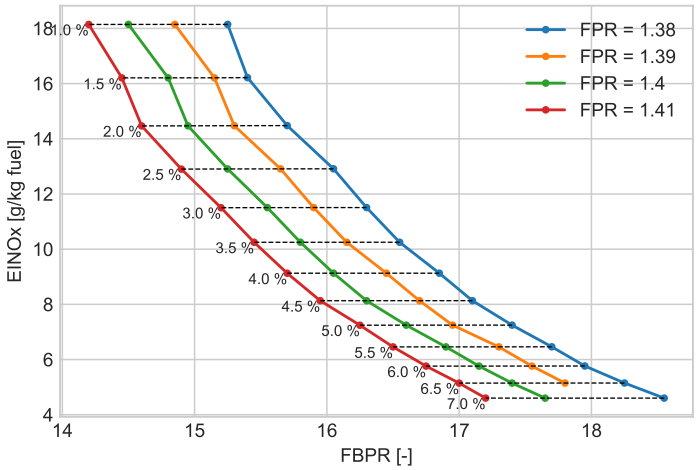

Figure 6.24: EINOx versus fan bypass ratio at different fan pressure ratio and WAR values.

The evaporator effectiveness, in Figure 6.25a, shows a small decrease at higher FPR and fixed WAR. The specific work of the LPT does not change as a result of the higher FPR and lower FBPR. The small effectiveness reduction is due to the increased core mass flow, which results in an increased water flow. Because both streams in the evaporator are changing mass flow proportionally, the resulting heat transfer rate increases by a small amount with higher FPR, seen in 6.25b.

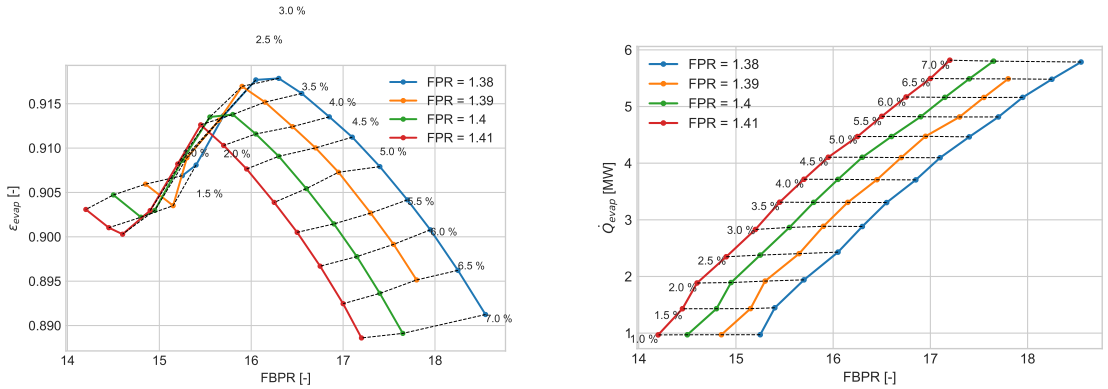

(a) Evaporator effectiveness vs fan bypass ratio for different fan pressure ratio and WAR values.

(b) Evaporator total heat transfer rate vs fan bypass ratio for different fan pressure ratio and WAR values.

Figure 6.25: Evaporator performance at varying fan pressure ratio and WAR.

The condenser performance, shown in 6.26 is directly influenced by the FPR. The effectiveness is reduced with increase in FPR at all fixed WAR values. The higher PR leads to a cooling air with higher temperature and in this model the lower FBPR reduces the mass flow at a constant CBPR. This has the same influence on the total heat transfer rate: Figure 6.26b.

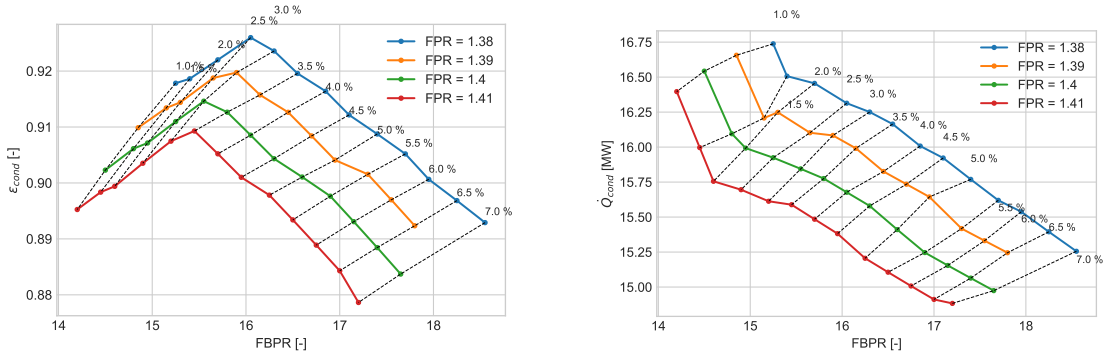

(a) Condenser effectiveness vs fan bypass ratio for different fan pressure ratio and WAR values.

(b) Condenser total heat transfer rate vs fan bypass ratio for different fan pressure ratio and WAR values.

Figure 6.26: Condenser performance at varying fan pressure ratio and WAR.

Figure 6.27 shows the water loop mass flows for varying FPR and WAR. The amount of water created in the condenser is less with increase in FPR, as seen in figure 6.27a. With higher FPR the threshold at which water is condensed is at a lower FBPR and at a higher WAR. The pressure and temperature of the exhaust gases does not change significantly, meaning the reduced condenser performance is due to a smaller temperature drop of the humid exhaust gases through the condenser. The reduced rate of water condensation with the increased core size leads to a higher requirement to supplement the engine with additional water, shown in Figure 6.27b.

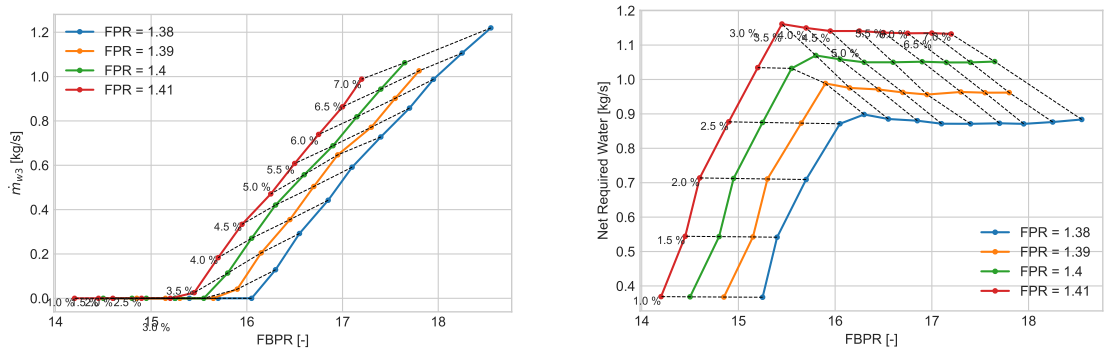

(a) Condenser liquid water mass flow output vs fan bypass ratio for different fan pressure ratio and WAR values.

(b) Required water to sustain water loop vs fan bypass ratio for different fan pressure ratio and WAR values.

Figure 6.27: Water cycle mass flow for varying fan pressure ratio and WAR.

7

Conclusion

The Steam Injected Water Recovering Turbofan was modeled in NPSS and a sweep of design conditions were run, varying WAR, FBPR, OPR, T_4, and FPR. The engine concept shows promise in simultaneously reducing fuel consumption and NOx emissions.

Answers to research questions

1. What is the performance improvement of the steam-injected turbofan over a comparable conventional turbofan?

    - How does the thrust-specific fuel consumption change?
      The thrust specific fuel consumption is reduced by up to 8% at WAR = 7%.
    - What are the relevant parameters that affect the performance of this engine?
      The water to air ratio (WAR) is the main relevant design parameter of this engine. At a fixed WAR, the concept displays design trends similar to a conventional turbofan, when the following design parameters are varied: FBPR, OPR, T_4, and FPR.

2. How are emissions influenced by the implementation of such a cycle over the same mission?

    - What are the NO_x emissions?
      EINOx can be reduced by up to 66% at WAR = 7%.

7.1. Conclusions

- The cycle allows for the use of bypass ratios above 20 by shrinking the core and keeping the fan size similar to a conventional turbofan. This makes it promising for use in new aircraft designed also for turbofans or retrofitting to existing aircraft.
- At top of climb, condensing enough water to supply what needs to be injected is difficult and likely impossible without using more of the bypass flow for cooling in the condenser. The larger FBPR provides more cooling flow and has a lower water requirement.
- A higher FBPR means that a larger portion of the thrust is generated by the bypass flow. This leads to an increase in propulsive efficiency, which is beneficial for overall cycle efficiency. Additionally, a high FBPR means that the FPR can be reduced, allowing for a colder cooling flow in the condenser.
- FPR has a direct effect on the performance of the condenser and ,should therefore be minimized, which can only be done by increasing FBPR. Fortunately, the SIWRT is very suitable for doing that, especially at much higher WAR or T_4.
- The simulation was unable to reach high water to air ratio solutions, the maximum achieved was 7%. The trends show further potential for performance improvement at higher WAR.
- WAR is a useful balance design parameter to reduce NOx emissions when a design choice otherwise would lead to an increase in NOx. If WAR values above 7% are achieved, the trends show a more significant reduction in SFC and NOx, making the argument that the added complexity of this cycle may be worth the performance gains.
- The steam turbine provides negligible power gains. The added complexity and weight of the component is not worth it for the design studied in this report. In the baseline, it was constrained by the quality of the injected steam. At higher T_4, it was severely constrained by the pressure requirement of the injected steam.

- The condensation of water appears to follow a linear correlation with WAR. In order to change the net production of water, changing the design WAR is not sufficient. Changes in engine and/or heat exchanger design are required. This provides a good potential for extremely high WAR values as any extra water in the exhaust gases can potentially be condensed back into the cycle. It is important to note that there likely exists a physical limit to extremely high WAR where this linear behavior may change.

7.2. Modeling and simulation points of attention

This section goes over the main points of what was learned in the creation of this simulation model.

- The mixer component which combines the cooling and remaining bypass flows after the condenser is likely the reason for the difficulty of convergence at higher WAR values. For modeling purposes, the added accuracy of mixing the flows is not worth the expense of solver convergence.
- The variable Cp-NTU 0D method used in the evaporator and condenser provides good result convergence for values with high evaporator effectiveness. A drawback of not simulating the streams in 1D is that the method suffers from low stability when discontinuities , such as phase change, are present.

7.3. Future work

This section describes future work and improvements to the model that are most important.

- Run the engine model at higher humidity values. Since the WAR values studied show a clear performance improvement, it is important to find the point of diminishing returns where a further increase in humidity is no longer as beneficial.
- Split the evaporator into 3 different component heat exchangers that can use the same modified NTU method. Each corresponding component only uses one of the respective phases: liquid, dual-phase, and vapor. NPSS has the option to create assemblies, which allows the user to create a sub-model containing multiple components within. This way the assembly can be inserted into the main model and is treated as a component by the main model.
- Run off-design simulations, namely: cruise and take-off. Cruise provides good potential for condensing more water than is needed in the cycle, which can be used to simultaneously fill the water tank and reduce contrails. While take-off is the most challenging condition for water condensation. Seeing the SIWRT's ability to sustain itself in those conditions is key to its overall feasibility.
- A way to utilize this cycle to its fullest would be the use of hydrogen fuel. The use of hydrogen in aviation is most beneficial when hydrogen is cryogenic, requiring a heat source prior to injection. Since exhaust gases require cooling to extract water, there is good synergy. In addition, exhaust gases from hydrogen combustion contain more water than kerosene combustion, which makes the condensation of water easier. Moreover, the stoichiometric flame temperature of hydrogen is significantly higher than that of kerosene, and steam injection can be used to reduce it to within the thermal limits of the materials.
- The limitation of the steam turbine is due to the requirement of overpressure of the steam injection. This can be circumvented by increasing the pressure rise in the water pump, which will allow more expansion in the turbine. Additionally, the system could potentially be matched to maximize heat transfer in the evaporator, as well as to exert as much work in the steam turbine as possible. This way, at even higher WAR, the generated power can be increased and the steam turbine could still be a viable addition to the engine without oversizing the heat exchangers.

References

[1] R. K. Mishra. "The Trend of Bypass Ratio in Aero Engines: An Overview". In: *Journal of Aerospace Sciences and Technologies* 74 (July 2022), pp. 79–89. ISSN: 2584-1351. DOI: 10.61653/JOAST.V74I2.2022.26. URL: https://www.joast.org/index.php/joast/article/view/26.

[2] F ; Yin, F S Tiemstra, and A Rao. "Development of a Flexible Turbine Cooling Prediction Tool for Preliminary Design of Gas Turbines". In: *Journal of Engineering for Gas Turbines and Power* 140 (9 2018). DOI: 10.1115/1.4039732. URL: https://doi.org/10.1115/1.4039732.

[3] Alan Epstein. *The Pratt Whitney PurePower ® Geared Turbofan™ Engine*. Sept. 2015.

[4] ICAO. "Wings of Prosperity: Economic Growth Through Air Transport". In: (First Edition Aug. 2024).

[5] ACI and ICAO. *Joint ACI World-ICAO Passenger Traffic Report, Trends, and Outlook | ACI World*. Jan. 2025. URL: https://aci.aero/2025/01/28/joint-aci-world-icao-passenger-traffic-report-trends-and-outlook/#.

[6] Dah Yu Cheng. "The Distinction Between the Cheng and STIG Cycles". In: *Proceedings of the ASME Turbo Expo* 4 (Sept. 2008), pp. 101–116. DOI: 10.1115/GT2006-90382. URL: https://dx.doi.org/10.1115/GT2006-90382.

[7] Dah Yu Cheng and Albert L.C. Nelson. "The chronological development of the Cheng cycle steam injected gas turbine during the past 25 years". In: *American Society of Mechanical Engineers, International Gas Turbine Institute, Turbo Expo (Publication) IGTI* 2 A (2002), pp. 421–428. DOI: 10.1115/GT2002-30119.

[8] Michel A. Saad and Dah Yu Cheng. "The new LM2500 Cheng cycle for power generation and cogeneration". In: *Energy Conversion and Management* 38 (15-17 Oct. 1997), pp. 1637–1646. ISSN: 0196-8904. DOI: 10.1016/S0196-8904(96)00204-X.

[9] Oliver Schmitz, Hermann Klingels, and Petra Kufner. "Aero Engine Concepts beyond 2030: Part 1-The Steam Injecting and Recovering Aero Engine". In: *Journal of Engineering for Gas Turbines and Power* 143 (2 Feb. 2021). ISSN: 15288919. DOI: 10.1115/1.4048985.

[10] Regina Pouzolz, Oliver Schmitz, and Hermann Klingels. "Evaluation of the climate impact reduction potential of the water-enhanced turbofan (WET) concept". In: *Aerospace* 8 (3 Mar. 2021), pp. 1–12. ISSN: 22264310. DOI: 10.3390/AEROSPACE8030059.

[11] Sascha Kaiser, Oliver Schmitz, Paul Ziegler, and Hermann Klingels. "The Water-Enhanced Turbofan as Enabler for Climate-Neutral Aviation". In: *Applied Sciences 2022, Vol. 12, Page 12431* 12 (23 Dec. 2022), p. 12431. ISSN: 2076-3417. DOI: 10.3390/APP122312431. URL: https://www.mdpi.com/2076-3417/12/23/12431.

[12] Paul Ziegler, Sascha Kaiser, and Volker Gümmer. "Parametric Cycle Studies of the Water-Enhanced Turbofan Concept". In: *Proceedings of the ASME Turbo Expo* 5 (June 2023). DOI: 10.1115/GT2023-100529.

[13] Sebastian Göke, Marc Füri, Gilles Bourque, Bernhard Bobusch, Katharina Göckeler, Oliver Krüger, Sebastian Schimek, Steffen Terhaar, and Christian Oliver Paschereit. "Influence of steam dilution on the combustion of natural gas and hydrogen in premixed and rich-quench-lean combustors". In: *Fuel Processing Technology* 107 (2013), pp. 14–22. ISSN: 03783820. DOI: 10.1016/J.FUPROC.2012.06.019.

[14] Richard Tuthill. "HUMID AIR TURBINE CYCLE TECHNOLOGY DEVELOPMENT PROGRAM". In: (July 2002). DOI: 10.2172/828955. URL: http://www.osti.gov/servlets/purl/828955-sJyb6y/native/.

[15] Sebastian Schimek, Sebastian Göke, and Christian Oliver Paschereit. "Emission formation of liquid fuel combustion under humidified conditions". In: *51st AIAA Aerospace Sciences Meeting including the New Horizons Forum and Aerospace Exposition 2013* (2013). DOI: 10.2514/6.2013-693.

[16] F.W. Meredith. "Cooling of Aircraft Engines". In: *Aeronautical Research Committee Reports and Memoranda No 1683* (Aug. 1935).

[17] *Numerical Propulsion System Simulation (NPSS) | SwRI*. URL: https://www.swri.org/consortia/numerical-propulsion-system-simulation-npss.

[18] Scott M. Jones. *An Introduction to Thermodynamic Performance Analysis of Aircraft Gas Turbine Engine Cycles Using the Numerical Propulsion System Simulation Code*. Mar. 2007. URL: http://www.sti.nasa.gov.

[19] Southwest Research Institute ®. "About Numerical Propulsion System Simulation (NPSS ®)". In: (Aug. 2020).

[20] J Häßy, J Schmeink, R Becker, S Reitenbach, M Vieweg, P Bekemeyer, and A Merle. "Hybrid Surrogate-Based Rubber Engine Model for Aircraft Multidisciplinary Design Optimization". In: *AIAA* (June 2020).

[21] Wolverine Ventures. "NPSS Basics".

[22] Long N Vu, Nandakumar Vijayakumar, and Donald R Wilson. "Overview of Studies using the Numerical Propulsion System Simulation at UT-Arlington". In: *AIAA Modeling and Simulation Technologies Conference* (Jan. 2018). DOI: 10.2514/6.2018-2162. URL: http://arc.aiaa.org.

[23] *NPSS Thermodynamics Guide*.

[24] Jeff Schutte, Jimmy C. Tai, and Dimitri N. Mavris. "Multi-design point cycle design incorporation into the environmental design space". In: *48th AIAA/ASME/SAE/ASEE Joint Propulsion Conference and Exhibit 2012*. 2012. ISBN: 9781600869358. DOI: 10.2514/6.2012-3812.

[25] John H Lienhard. *A Heat Transfer Textbook, Fifth Edition*. URL: http://ahtt.mit.edu.

[26] Amir Faghri and Yuwen Zhang. *Fundamentals of Multiphase Heat Transfer and Flow*. Springer International Publishing, Sept. 2019, pp. 1–820. ISBN: 9783030221379. DOI: 10.1007/978-3-030-22137-9/COVER.

[27] Piero Colonna, Emiliano Casati, Carsten Trapp, Tiemo Mathijssen, Jaakko Larjola, Teemu Turunen-Saaresti, and Antti Uusitalo. "Organic Rankine Cycle Power Systems: From the Concept to Current Technology, Applications, and an Outlook to the Future". In: *Journal of Engineering for Gas Turbines and Power* 137 (10 Oct. 2015). ISSN: 15288919. DOI: 10.1115/1.4029884/373802. URL: https://dx.doi.org/10.1115/1.4029884.

[28] C. J. Geankoplis, A. A. Hersel, and D.H. Lepek. *Transport Processes and Separation Processes Principles*. 2018.

[29] David Gordon Wilson and Theodosios Korakianitis. *The Design of High-Efficiency Turbomachinery and Gas Turbines second edition , with a new preface*. Second edition. The MIT Press, 2014, pp. 458–460. ISBN: 9780262526685. URL: https://mitpress.mit.edu/9780262526685/the-design-of-high-efficiency-turbomachinery-and-gas-turbines/.

[30] NASA. "Aeronautical technologies for the twenty-first century". In: (19930001459 1992).

[31] GasTurb Gmbh. *GasTurb 14 Design and Off-Design Performance of Gas Turbines*. 2024.

[32] W. S.Y. Hung. "ACCURATE METHOD OF PREDICTING THE EFFECT OF HUMIDITY OR INJECTED WATER ON NOx EMISSIONS FROM INDUSTRIAL GAS TURBINES." In: *American Society of Mechanical Engineers (Paper)* (74 -WA/GT-6 1974). ISSN: 04021215.

[33] D. S. Lee, D. W. Fahey, A. Skowron, M. R. Allen, U. Burkhardt, Q. Chen, S. J. Doherty, S. Freeman, P. M. Forster, J. Fuglestvedt, A. Gettelman, R. R. De León, L. L. Lim, M. T. Lund, R. J. Millar, B. Owen, J. E. Penner, G. Pitari, M. J. Prather, R. Sausen, and L. J. Wilcox. "The contribution of global aviation to anthropogenic climate forcing for 2000 to 2018". In: *Atmospheric Environment* 244 (Jan. 2021), p. 117834. ISSN: 1352-2310. DOI: 10.1016/J.ATMOSENV.2020.117834.

[34] Rui Xu, Hai Wang, Med Colket, and Tim Edwards. "Thermochemical Properties of Jet Fuels". In: (2015).

[35] U. Schumann. "On conditions for contrail formation from aircraft exhausts". In: *Meteoroligsche Zeitschrift* Vol.5 (Feb. 1996).

[36] Arnold E Anderson, Walter K Arnold, Royce N Brown, Dow Chemical, G Kenneth Budinski, and Ralph A Burton. *Friction, Lubrication, and Wear Technology*. Vol. 18. ASM International, 1992.

[37] Feijia Yin. "Modelling and Characteristics of a Novel Multi-fuel Hybrid Engine for Future Aircraft". PhD thesis. Delft University of Technology, Sept. 2016, p. 35. ISBN: 9789461867117. URL: https://www.researchgate.net/publication/322299242_Modelling_and_Characteristics_of_a_Novel_Multi-fuel_Hybrid_Engine_for_Future_Aircraft.

[38] Marc Schmeicher, Jannik Häßy, Alexander Görtz, and Mahmoud El-Soueidan. “Methods for the Preliminary Design of Heat Exchangers in Aircraft Engines”. In: German Aerospace Center (DLR), Cologne, Germany, June 2023.

[39] Anders Lundbladh and Anders Sjunnesson. “Heat Exchanger Weight and Efficiency Impact on Jet Engine Transport”. In: *ISABE-2003-1122* (2003).

A

SIWRT data

This appendix is for additional data on the SIWRT. Design parameters are given in Table A.1. Only parameters, different than the RM400 are given. Figure A.2 shows the component pressure drop values.

Table A.1: SIWRT engine data. Only the parameters different to the RM400 are given.

	Value	Units
OPR	48	-
T_4	1700	K
CBPR	5	-
PR_{fan}	1.4	-
PR_{HPC}	10.76	
dP_{pump}	80	bar
η_{pump}	0.8	
$\eta_{st.turb}$	0.87	
UAh_{evap}	27.61	W/K
UAh_{cond}	168.4	W/K

Table A.2: SIWRT pressure drop values for ducts and components. Components and ducts have the same pressure drop values as the RM400, but may have different station nomenclature, thus they are included.

Components	Station	Pressure ratio
steam injector	P_{31}/P_{3a}	0.98
combustor	P_4/P_{31}	0.95
condenser cooling flow	P_{174}/P_{171}	0.95
condenser exhaust gas	P_{61}/P_6	0.9
evaporator water flow	P_{w2}/P_{w15}	0.95
evaporator exhaust gas	P_6/P_{55}	0.9
Ducts		
inlet	P_2/P_1	0.998
core fan to LPC	P_{22}/P_{21}	0.99
inter compressor	P_{25}/P_{24}	0.99
inter turbine	P_{445}/P_{44}	0.99
LPT to evaporator	P_{55}/P_{50}	0.99
BP fan to condenser	P_{17}/P_{15}	0.99

A.1. SIWRT complete diagram

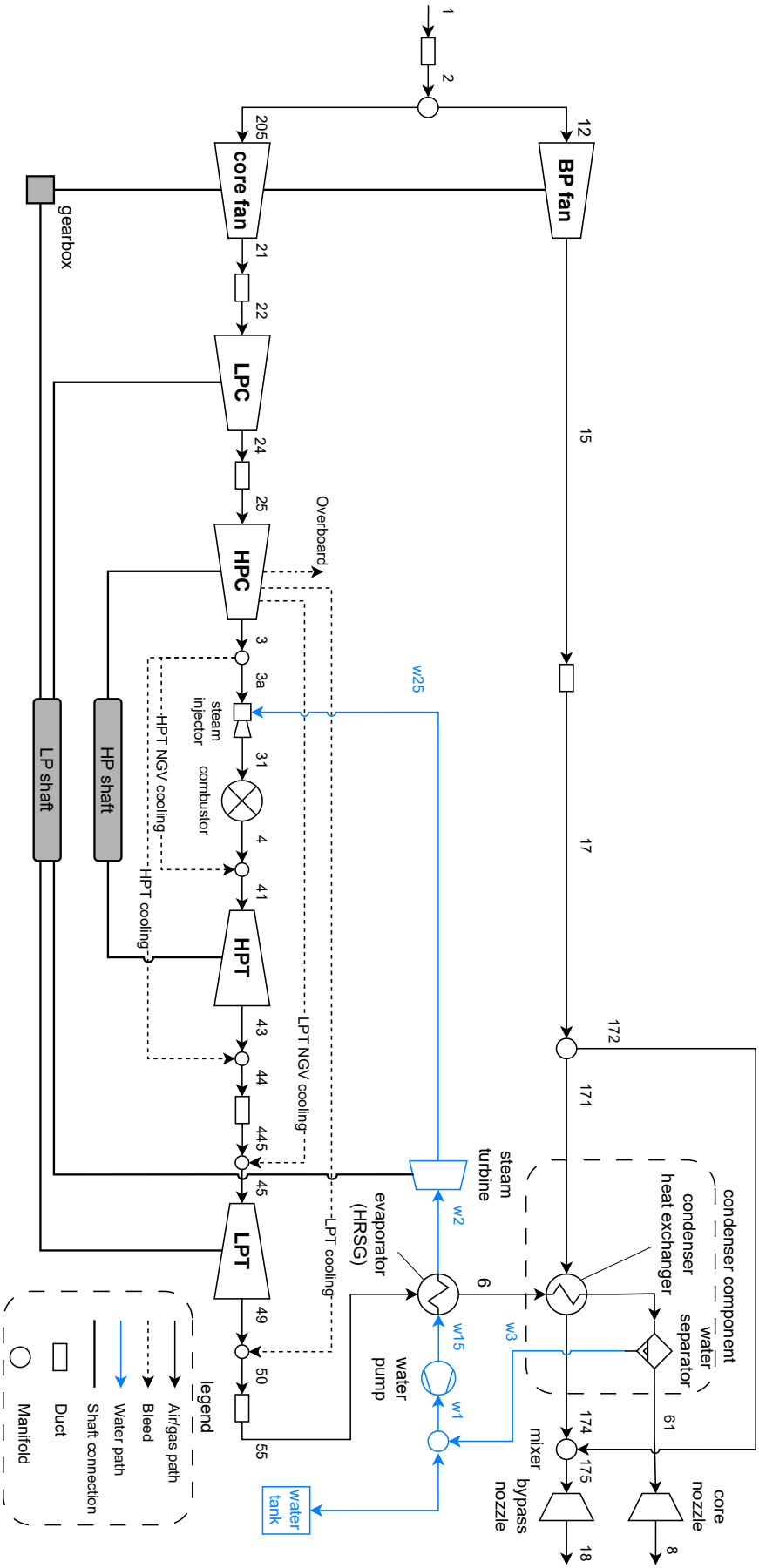

Figure A.1: SIWRT complete diagram with station notation, bleed ports, and ducts.

B

RM-400 Engine

The RM-400 engine is a ultra-high bypass ratio turbofan engine, intended for entry into service in 2035. The design follows existing turbofan evolution trends that increase FBPR to maximize propulsive efficiency. In this study, the RM-400 is used as a reference engine, which the SIWRT can be compared to. Table B.1 shows the design parameters of the RM400, Table B.2 shows component efficiency values, Table B.3 shows the bleed values, and Table B.4 shows the pressure drop of all components and ducts that have any.

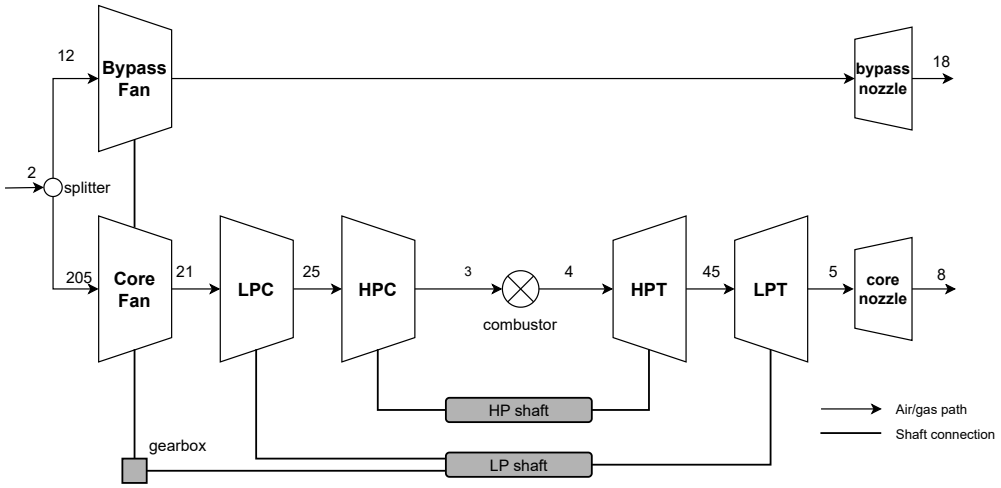

Figure B.1: Diagram of the RM400 with station nomenclature.

B.1. Specifications

Table B.1: RM-400 engine specifications

OPR	74	-
T_4	1903.77	K
FBPR	13.7	-
$PR_{BP\ fan}$	1.44	-
$PR_{core\ fan}$	1.3	-
PR_{LPC}	3.5	-
PR_{HPC}	16.59	-
PR_{HPT}	4.86	-
PR_{LPT}	10.53	-
Gearbox gear ratio	3.61	-
Fuel	Kerosene	
LHV	43	MJ/kg
$\dot{m}_{corr,inlet}$	1602.26	kg/s
$\dot{m}_{inlet}$	627.47	kg/s

B.1.1. Component efficiency

Table B.2: RM-400 component efficiency values. Turbomachinery isentropic efficiency values are given.

$\eta_{BP\ fan}$	0.9158
$\eta_{core\ fan}$	0.8754
η_{LPC}	0.8872
η_{HPC}	0.8695
η_{HPT}	0.93
η_{LPT}	0.935
η_{comb}	0.9995

B.1.2. Bleed flow

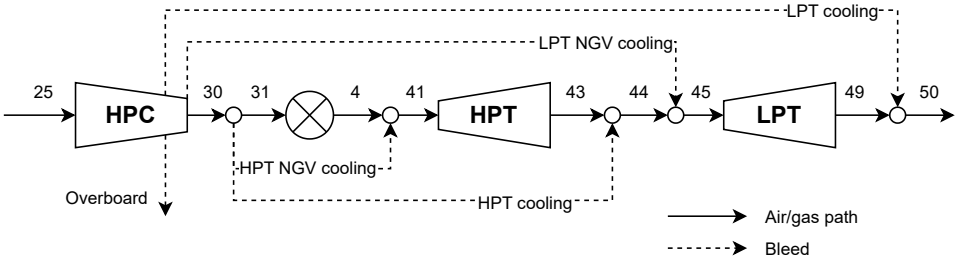

Figure B.2: RM400 bleed flows with station numbers.

Table B.3: RM-400 bleed values.

Bleed type	amount	
Overboard	0.839146	kg/s
LPT cooling	0.125	%
LPT NGV	1.875	%
HPT cooling	3.1	%
HPT NGV	17.7	%

Table B.4: RM400 pressure drop values for ducts and components.

Components	Station	Pressure ratio
combustor	P_4/P_{31}	0.95
Ducts		
inlet	P_2/P_1	0.998
core fan to LPC	P_{22}/P_{21}	0.99
inter compressor	P_{25}/P_{24}	0.99
inter turbine	P_{445}/P_{44}	0.99
LPT to evaporator	P_{55}/P_{50}	0.99
BP fan to condenser	P_{17}/P_{15}	0.99

B.1.3. Pressure drop

B.2. Performance

Table B.5: RM-400 performance data.

F_{net}	67.35	kN
$\dot{m}_{fuel}$	0.953	kg/s
SFC	14.15	kg/s-kN
NO_x	31.09	g/kg

B.3. Verification

The RM400 started as a GasTurb 13 model which was transferred into NPSS to act as the basis for SIWRT. B.3 shows the verification results as difference in main parameter values. The largest deviation is the fuel mass flow and (T)SFC of 1%. This is likely due to a difference in the burner models, however NPSS does no provide the inner workings of the burn mechanics. In the end this difference was deemed acceptable as the comparison of the RM400 and the SIWRT was done entirely in NPSS, so no such difference is introduced to the comparisons in this report.

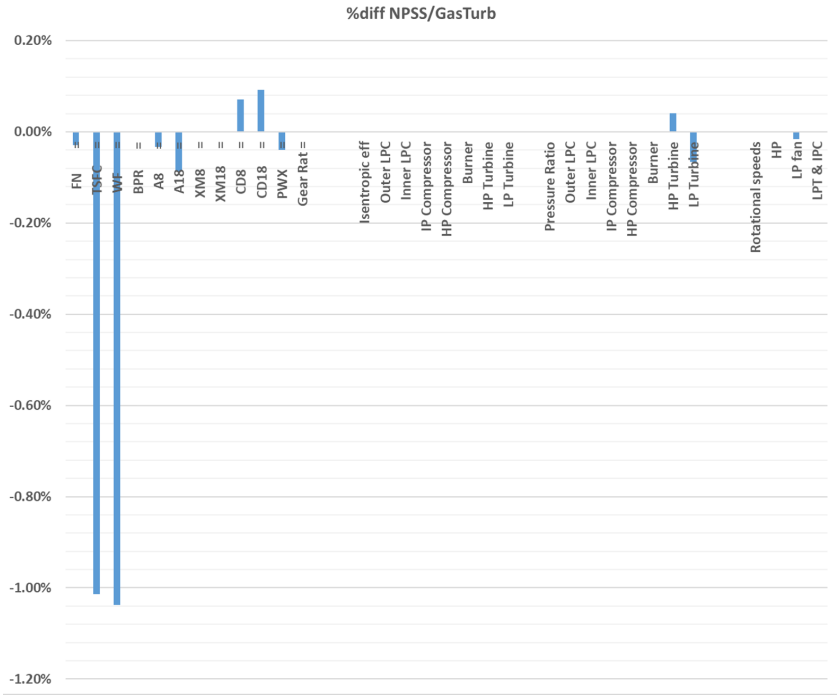

Figure B.3: RM-400 NPSS model verification against GasTurb 12.

B.4. Validation

The RM400 could not be validated with experimental or operational data as it is a future concept that does not exist.

C

Chemistry data

This appendix provides the chemistry data that was used in the study.

C.1. Species

Janaf thermopackage uses the 17 species. They are shown in Table C.1 with their molar mass and enthalpy of formation provided by NPSS.

Table C.1: Species used in Janaf thermopackage with their molar mass and enthalpy of formation.

Janaf species at T_{ref} = 298.15 K, P_{ref} = 101325 Pa					
#	specie	M [g/mol]	h_f [kJ/mol]	h_f [kJ/kg]	h_f [Btu/lbm]
1	H_2O	18.0153	-241.8452	-13424.4	-5771.48
2	CO_2	44.0098	-393.5442	-8942.2	-3844.46
3	O_2	31.9988	0	0	0
4	N_2	28.0135	0	0	0
5	Ar	39.948	0	0	0
6	CH_4O	32.0422	-201.0126	-6273.37	-2697.07
7	NH_3	17.0306	-45.90286	-2695.32	-1158.78
8	H_2	2.01588	0	0	0
9	O	15.9994	249.18549	15574.68	6695.92
10	H	1.00794	218.01353	216296.1	92990.8
11	CO	28.0104	-110.537	-3946.28	-1696.6
12	OH	17.0073	38.992413	2292.687	985.68
13	NO	30.0061	90.295342	3009.233	1293.74
14	N	14.0067	472.70922	33748.79	14509.4
15	CH_4	16.0428	-74.60483	-4650.36	-1999.3
16	C_2H_4	28.0538	52.503217	1871.519	804.61
17	$C_{10}H_8$	128.174	150.5895	1174.883	505.11

The data is extracted from NPSS, where it is stored in imperial units. Any used in this study use the NPSS conversion factors shown in Table C.2:

C.2. Gas mixtures

The properties of gas mixtures are determined by the individual species' properties and their mass fractions:

Table C.2: Unit conversion factors provided by NPSS.

SI	Imperial	Factor
kg	lbm	2.20462
m	ft	3.28084
K	R	1.8
kJ	Btu	0.947818
MPa	psia	145.038

Mean molar mass is given by:

$$\frac{\mathbf{1}}{\overline{\mathbf{M}}} = \sum_{\mathbf{k}} \frac{\mathbf{q^k}}{\mathbf{M^k}} \tag{C.1}$$

Mean total specific enthalpy is given by:

$$\frac{\mathbf{1}}{\overline{\mathbf{h}}} = \sum_{\mathbf{k}} \frac{\mathbf{q^k}}{\mathbf{h^k}} \tag{C.2}$$

Mean total specific entropy is given by:

$$\frac{\mathbf{1}}{\overline{\mathbf{s}}} = \sum_{\mathbf{k}} \frac{\mathbf{q^k}}{\mathbf{s^k}} \tag{C.3}$$

Mean density is given by:

$$\frac{\mathbf{1}}{\overline{\rho}} = \sum_{\mathbf{k}} \frac{\mathbf{q^k}}{\rho^{\mathbf{k}}} \tag{C.4}$$

Mean isochoric specific heat is given by:

$$\frac{\mathbf{1}}{\overline{\mathbf{Cv}}} = \sum_{\mathbf{k}} \frac{\mathbf{q^k}}{\mathbf{Cv^k}} \tag{C.5}$$

Mean isobaric specific heat is given by:

$$\frac{\mathbf{1}}{\overline{\mathbf{Cp}}} = \sum_{\mathbf{k}} \frac{\mathbf{q^k}}{\mathbf{Cp^k}} \tag{C.6}$$

Mean specific heat ratio is given by:

$$\frac{\mathbf{1}}{\overline{\gamma}} = \sum_{\mathbf{k}} \frac{\mathbf{q^k}}{\gamma^{\mathbf{k}}} \tag{C.7}$$

C.3. Air composition

The default air composition given in species mass fractions is shown in Table C.3:

Table C.3: Janaf species and default dry air and humid air composition as species mass fractions.

#	specie	mass fraction q	
		dry	humid
1	H_2O	0	$\frac{WAR}{WAR+1}$
2	CO_2	0.000484	$\frac{0.000484}{WAR+1}$
3	O_2	0.231416	$\frac{0.231416}{WAR+1}$
4	N_2	0.7555184	$\frac{0.7555184}{WAR+1}$
5	Ar	0.012916	$\frac{0.012916}{WAR+1}$
6	CH_4O	0	0
7	NH_3	0	0
8	H_2	0	0
9	O	0	0
10	H	0	0
11	CO	0	0
12	OH	0	0
13	NO	0	0
14	N	0	0
15	CH_4	0	0
16	C_2H_4	0	0
17	$C_{10}H_8$	0	0